




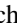
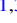



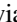










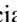




















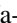














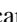














A DECam Search for Explosive Optical Transients Associated with IceCube Neutrino Alerts

R. Morgan^{1,2} , K. Bechtol^{1,3} , R. Kessler^{4,5} , M. Sako⁶ , K. Herner⁷ , Z. Doctor⁵ , D. Scolnic⁵ , I. Sevilla-Noarbe⁸ ,
 A. Franckowiak⁹ , K. N. Neilson¹⁰ , M. Kowalski^{11,12} , A. Palmese⁷ , E. Swann¹³ , B. P. Thomas¹³ , A. K. Vivas¹⁴ ,
 A. Drlica-Wagner^{5,7} , A. Garcia¹⁵ , D. Brout⁶ , F. Paz-Chinchón¹⁶ , E. Neilsen⁷ , H. T. Diehl⁷ , M. Soares-Santos¹⁵ ,
 T. M. C. Abbott¹⁴ , S. Avila¹⁷ , E. Bertin^{18,19} , D. Brooks²⁰ , E. Buckley-Geer⁷ , A. Carnero Rosell^{8,21} , M. Carrasco Kind^{16,22} ,
 J. Carretero²³ , R. Cawthon²⁴ , M. Costanzi²⁵ , J. De Vicente⁸ , S. Desai²⁶ , P. Doel²⁰ , B. Flaugher⁷ , P. Fosalba^{27,28} ,
 J. Frieman^{5,7} , J. García-Bellido¹⁷ , E. Gaztanaga^{27,28} , D. W. Gerdes^{29,30} , D. Gruen^{31,32,33} , R. A. Gruendl^{16,22} ,
 J. Gschwend^{21,34} , G. Gutierrez⁷ , D. L. Hollowood³⁵ , K. Honscheid^{36,37} , D. J. James³⁸ , N. Kuropatkin⁷ , M. Lima^{21,39} ,
 M. A. G. Maia^{21,34} , J. L. Marshall⁴⁰ , F. Menanteau^{16,22} , C. J. Miller^{29,30} , R. Miquel^{23,41} , A. A. Plazas⁴² , E. Sanchez⁸ ,
 V. Scarpine⁷ , M. Schubnell³⁰ , S. Serrano^{27,28} , M. Smith⁴³ , F. Sobreira^{21,44} , E. Suchyta⁴⁵ , M. E. C. Swanson¹⁶ , G. Tarle³⁰ ,
 V. Vikram⁴⁶ , A. R. Walker¹⁴ , and J. Weller^{25,47,48} 

¹ Physics Department, University of Wisconsin-Madison, 1150 University Avenue Madison, WI 53706, USA; robert.morgan@wisc.edu, kbechtol@wisc.edu

² Large Synoptic Survey Telescope Corporation Data Science Fellowship Program, USA

³ Large Synoptic Survey Telescope, 933 North Cherry Avenue, Tucson, AZ 85721, USA

⁴ Department of Astronomy and Astrophysics, University of Chicago, Chicago, IL 60637, USA

⁵ Kavli Institute for Cosmological Physics, University of Chicago, Chicago, IL 60637, USA

⁶ Department of Physics and Astronomy, University of Pennsylvania, Philadelphia, PA 19104, USA

⁷ Fermi National Accelerator Laboratory, P.O. Box 500, Batavia, IL 60510, USA

⁸ Centro de Investigaciones Energéticas, Medioambientales y Tecnológicas (CIEMAT), Madrid, Spain

⁹ Deutsches Elektronen Synchrotron DESY, D-15738 Zeuthen, Germany

¹⁰ Department of Physics, Drexel University, 3141 Chestnut St, Philadelphia, PA 19104, USA

¹¹ Institute of Physics, Humboldt-Universität zu Berlin, Newtonstr. 15, D-12489 Berlin, Germany

¹² Deutsches Elektronen-Synchrotron, D-15735 Zeuthen, Germany

¹³ Institute of Cosmology and Gravitation, University of Portsmouth, Portsmouth, PO1 3FX, UK

¹⁴ Cerro Tololo Inter-American Observatory, National Optical Astronomy Observatory, Casilla 603, La Serena, Chile

¹⁵ Brandeis University, Physics Department, 415 South Street, Waltham MA 02453, USA

¹⁶ National Center for Supercomputing Applications, 1205 West Clark St., Urbana, IL 61801, USA

¹⁷ Instituto de Física Teórica UAM/CSIC, Universidad Autónoma de Madrid, E-28049 Madrid, Spain

¹⁸ CNRS, UMR 7095, Institut d'Astrophysique de Paris, F-75014, Paris, France

¹⁹ Sorbonne Universités, UPMC Univ Paris 06, UMR 7095, Institut d'Astrophysique de Paris, F-75014, Paris, France

²⁰ Department of Physics & Astronomy, University College London, Gower Street, London, WC1E 6BT, UK

²¹ Laboratório Interinstitucional de e-Astronomia—LIneA, Rua Gal. José Cristino 77, Rio de Janeiro, RJ—20921-400, Brazil

²² Department of Astronomy, University of Illinois at Urbana-Champaign, 1002 W. Green Street, Urbana, IL 61801, USA

²³ Institut de Física d'Altes Energies (IFAE), The Barcelona Institute of Science and Technology, Campus UAB, E-08193 Bellaterra (Barcelona), Spain

²⁴ Physics Department, 2320 Chamberlin Hall, University of Wisconsin-Madison, 1150 University Avenue Madison, WI 53706-1390, USA

²⁵ Universitäts-Sternwarte, Fakultät für Physik, Ludwig-Maximilians-Universität München, Scheinerstr. 1, D-81679 München, Germany

²⁶ Department of Physics, IIT Hyderabad, Kandi, Telangana 502285, India

²⁷ Institut d'Estudis Espacials de Catalunya (IEEC), E-08034 Barcelona, Spain

²⁸ Institute of Space Sciences (ICE, CSIC), Campus UAB, Carrer de Can Magrans, s/n, 08193 Barcelona, Spain

²⁹ Department of Astronomy, University of Michigan, Ann Arbor, MI 48109, USA

³⁰ Department of Physics, University of Michigan, Ann Arbor, MI 48109, USA

³¹ Department of Physics, Stanford University, 382 Via Pueblo Mall, Stanford, CA 94305, USA

³² Kavli Institute for Particle Astrophysics & Cosmology, P.O. Box 2450, Stanford University, Stanford, CA 94305, USA

³³ SLAC National Accelerator Laboratory, Menlo Park, CA 94025, USA

³⁴ Observatório Nacional, Rua Gal. José Cristino 77, Rio de Janeiro, RJ—20921-400, Brazil

³⁵ Santa Cruz Institute for Particle Physics, Santa Cruz, CA 95064, USA

³⁶ Center for Cosmology and Astro-Particle Physics, The Ohio State University, Columbus, OH 43210, USA

³⁷ Department of Physics, The Ohio State University, Columbus, OH 43210, USA

³⁸ Center for Astrophysics, Harvard & Smithsonian, 60 Garden Street, Cambridge, MA 02138, USA

³⁹ Departamento de Física Matemática, Instituto de Física, Universidade de São Paulo, CP 66318, São Paulo, SP, 05314-970, Brazil

⁴⁰ George P. and Cynthia Woods Mitchell Institute for Fundamental Physics and Astronomy, and Department of Physics and Astronomy, Texas A&M University, College Station, TX 77843, USA

⁴¹ Institució Catalana de Recerca i Estudis Avançats, E-08010 Barcelona, Spain

⁴² Department of Astrophysical Sciences, Princeton University, Peyton Hall, Princeton, NJ 08544, USA

⁴³ School of Physics and Astronomy, University of Southampton, Southampton, SO17 1BJ, UK

⁴⁴ Instituto de Física Gleb Wataghin, Universidade Estadual de Campinas, 13083-859, Campinas, SP, Brazil

⁴⁵ Computer Science and Mathematics Division, Oak Ridge National Laboratory, Oak Ridge, TN 37831, USA

⁴⁶ Argonne National Laboratory, 9700 South Cass Avenue, Lemont, IL 60439, USA

⁴⁷ Excellence Cluster Origins, Boltzmannstr. 2, 85748 Garching, Germany

⁴⁸ Max Planck Institute for Extraterrestrial Physics, Giessenbachstrasse, 85748 Garching, Germany

Received 2019 July 15; revised 2019 August 8; accepted 2019 August 9; published 2019 September 26

Abstract

In this work, we investigate the likelihood of association between real-time, neutrino alerts with teraelectronvolt to petaelectronvolt energy from IceCube and optical counterparts in the form of core-collapse supernovae (CC SNe). The optical follow-up of IceCube alerts requires two main instrumental capabilities: (1) deep imaging, since 73%

of neutrinos would come from CC SNe at redshifts $z > 0.3$, and (2) a large field of view (FoV), since typical IceCube muon neutrino pointing accuracy is on the order of ~ 1 deg. With Blanco/DECam (*gri* to 24th magnitude and 2.2 deg diameter FoV), we performed a triggered optical follow-up observation of two IceCube alerts, IC170922A and IC171106A, on six nights during the three weeks following each alert. For the IC170922A (IC171106A) follow-up observations, we expect that 12.1% (9.5%) of coincident CC SNe at $z \lesssim 0.3$ are detectable, and that, on average, 0.23 (0.07) unassociated SNe in the neutrino 90% containment regions also pass our selection criteria. We find two candidate CC SNe that are temporally coincident with the neutrino alerts in the FoV, but none in the 90% containment regions, a result that is statistically consistent with expected rates of background CC SNe for these observations. If CC SNe are the dominant source of teraelectronvolt to petaelectronvolt neutrinos, we would expect an excess of coincident CC SNe to be detectable at the 3σ confidence level using DECam observations similar to those of this work for ~ 60 (~ 200) neutrino alerts with (without) redshift information for all candidates.

Unified Astronomy Thesaurus concepts: Core-collapse supernovae (304); Neutrino astronomy (1100); Optical observation (1169)

1. Introduction

The detection of astrophysical neutrinos with teraelectronvolt to petaelectronvolt energy with the IceCube detector (IceCube Collaboration 2013) has opened a door for multi-messenger studies of energetic astrophysical environments (Franckowiak 2017). Such high-energy neutrinos are generally understood to be produced exclusively by the interaction of hadrons that have been accelerated to high energies (Abbasi et al. 2011). Neutrinos are largely unaffected by intervening matter and radiation fields and thus can carry information from larger redshifts, and from deeper within opaque sources, than any other particle messenger (Chiarusi & Spurio 2010; Baret & Elewycyk 2011). These properties make teraelectronvolt to petaelectronvolt energy neutrinos informative probes of high-energy environments, with the potential to provide unique insight into explosive events, such as supernovae (Gaisser & Stanev 1987) and active galaxies (Silberberg & Shapiro 1979), across cosmic time.

In neutrino astronomy, the low neutrino interaction cross section limits the event rate of high-confidence astrophysical neutrinos to a few events per year (Aartsen et al. 2017a). To enable time-domain searches for counterparts to the detected astrophysical neutrinos, the IceCube Collaboration has implemented a real-time alert system for the highest confidence and best-localized neutrino events. Twenty-two public real-time neutrino alerts have been issued since 2016 (IceCube Collaboration 2018a), leading to the identification of the first compelling electromagnetic counterpart of a teraelectronvolt-energy neutrino, the flaring gamma-ray blazar TXS 0506+056 (IceCube Collaboration 2018b; IceCube Collaboration et al. 2018). We discuss the connection of TXS 0506+056 to this work in Section 3. The sources of the other 21 alerts remain unknown.

The observed flux for all astrophysical neutrinos with teraelectronvolt to petaelectronvolt energies is nearly isotropic, supporting a primarily extragalactic origin (Aartsen et al. 2015a; Ahlers et al. 2016). Several prominent nonthermal and extragalactic source classes, including gamma-ray bursts (Aartsen et al. 2015c), gamma-ray blazars (Aartsen et al. 2017c), and star-forming galaxies (Bechtol et al. 2017), have been suggested and now have stringent upper limits on their total contributions to the IceCube signal. Many analyses have proposed that a subset of core-collapse supernovae (CC SNe) have internal jets or shocks that produce prompt teraelectronvolt to petaelectronvolt neutrino emission (Thompson et al. 2003; Razzaque et al. 2004; Ando & Beacom 2005; Woosley & Janka 2005; Murase & Ioka 2013, among several others).

In this work, we investigate the possibility of determining observationally whether CC SNe contribute to the teraelectronvolt to petaelectronvolt energy neutrino flux via a prompt neutrino emission mechanism. In order to identify a CC SN associated with a neutrino alert, a follow-up of the event must begin as soon as possible after the neutrino signal has been observed. This should happen ideally within 1–2 days because some explosion models predict a fast-rising electromagnetic flux on the order of days (González-Gaitán et al. 2015). Note that the rise times of SN explosion models are relatively unconstrained, so the precise determination of the explosion time from observations is challenging. Additionally, the high matter densities in collapsing stars are expected to be opaque to gamma rays (Mészáros & Waxman 2001; Dermer & Atoyan 2003; Senno et al. 2016; Tamborra & Ando 2016), meaning the neutrino signal would lack an accompanying gamma-ray burst. SNe, though, are characteristically bright in the optical bands despite the cosmological distances. Therefore, triggered optical follow-up of the best-localized IceCube neutrino events is an attractive way to search for CC SNe in coincidence with individual neutrino sources (Kowalski & Mohr 2007). We discuss the physical model on which we base our search and its underlying assumptions in Section 2.

For optical follow-up to be feasible, the instrument field of view (FoV) must be matched to the solid angle on the sky containing the neutrino in 90% of cases (the 90% confidence level containment region) such that there is a high probability of capturing the neutrino source without becoming overwhelmed by false positives. The median angular resolution for neutrinos detected by IceCube with energies above 100 TeV is less than 1° (Aartsen et al. 2017d). In addition, the neutrino emission from CC SNe is expected to follow the cosmic star formation rate, in which case the majority of neutrinos detected at the Earth would be produced by distant sources (Strigari et al. 2005). Therefore, the instrument must also reach an imaging depth sufficient to observe the faint optical signal of the distant CC SNe. This scenario has motivated several optical follow-up efforts, including programs with the Robotic Optical Transient Search Experiment (ROTSE) and the Palomar Transient Factory (PTF) that reach typical limiting magnitudes of 17 and 21, respectively (Abbasi et al. 2012; Aartsen et al. 2015b). The most recent optical follow-up was performed by Pan-STARRS1 (limiting magnitude ~ 22.5 , Kankare et al. 2019) in which none of the transient sources found close in direction to five IceCube alerts had convincing evidence for an association. One plausible explanation for the lack of neutrino

candidates found by these studies is their low sensitivity to faint, distant objects. We elaborate on the need for deep imaging in Section 6. One of the primary goals of this work is to quantify the sensitivity of optical follow-up campaigns to a teraelectronvolt to petaelectronvolt neutrino-emitting CC SN. In this work, we present the deepest optical follow-up to date of IceCube alerts and go beyond the scope of previous studies by characterizing the sensitivity of our follow-up campaign via a maximum-likelihood analysis of SNe simulations.

On 2017 September 22 and 2017 November 6, we received alerts for individual ~ 200 TeV neutrinos detected by IceCube with good localization and high probability to be of astrophysical origin (IC170922A and IC171106A, respectively). We used the Dark Energy Camera (DECam) mounted on the 4 m Blanco Telescope in Chile to perform triggered optical follow-up of the two IceCube neutrino alerts. Blanco/DECam's 2.2 deg diameter FoV was able to cover the entire 90% confidence level containment regions in a single pointing for each alert and reached a limiting r -band magnitude of 23.6 mag for a 5σ detection, allowing for a higher sensitivity to CC SNe out to larger redshifts compared to previous efforts. The details of our follow-up observations are presented in Section 3.

As a result of the wide FoV and imaging depth, DECam is capable of finding several hundred transient objects per follow-up. Therefore, to expedite the screening procedure and standardize the selection methodology, in Section 4 we present an automated candidate selection pipeline for CC SNe exploding at the time of the neutrino alert. We apply the pipeline to our observations and present the results in Section 5. In Section 6 we supplement our pipeline with calculations of the likelihood of association between a neutrino alert and a likely CC SN selected by the pipeline. We also describe the requirements of an optical follow-up campaign capable of determining whether CC SNe contribute to the teraelectronvolt to petaelectronvolt IceCube neutrino flux at a high confidence level. We conclude in Section 7.

2. Physical Model

In this analysis, we evaluate the likelihood that teraelectronvolt to petaelectronvolt energy neutrinos detected by IceCube are created by a prompt emission mechanism during the collapse. We take this mechanism to be a relativistic jet within the collapsing massive star (Abbasi et al. 2012) such that hadrons within the star are boosted to teraelectronvolt to petaelectronvolt energies. The boost could be caused by several factors, such as shock breakout or the espresso mechanism (Caprioli 2015). Within the collapsing star, boosted protons could interact with photons, leading to the production of charged pions, which would decay to produce energetic neutrinos (Gaisser & Stanev 1987). The high-energy neutrinos then escape the collapsing star because of their low interaction cross section (Beall 2006). We make the assumption that the direction of the internal relativistic jet has no influence on our ability to detect the optical signal of the explosion.

With the above model for the explosion, the multimessenger signal detectable on Earth would consist of the teraelectronvolt to petaelectronvolt energy neutrino and the electromagnetic signature of a CC SN. The neutrino signal could be an individual neutrino or several neutrinos arriving close in time, a so-called neutrino multiplet. A multiplet indicates a closer source, because only in that case is the mean number of

expected neutrino events detected by IceCube expected to be larger than one. The majority of singular neutrino events come from more distant sources, with a mean number of expected neutrino events much smaller than one (IceCube Collaboration et al. 2017; Strotjohann et al. 2019). In this analysis, the alerts we followed up are single-neutrino alerts. The neutrino signal is expected to be detected on Earth a few hours to ~ 1 day before the electromagnetic signal becomes bright enough to be detectable. This time delay is a direct result of our assumed explosion mechanism: the neutrinos are emitted at the beginning of the explosion and nearly immediately escape the star, while photons are emitted throughout the typically week-scale process and have a much shorter mean free path between interactions inside the star. Furthermore, gamma rays created by the prompt neutrino mechanism have a high probability of being absorbed by the dense stellar material, so the dominant electromagnetic signal would be seen in the optical wavelength range with a delay of a few hours to ~ 1 day.

To test our hypothesis that CC SNe contribute to the teraelectronvolt to petaelectronvolt energy neutrino flux detected by IceCube, we perform a maximum-likelihood analysis of the objects found by Blanco/DECam during our triggered follow-up observations. For this analysis, we derive the expected redshift distributions of background SNe and associated CC SNe in Section 4. Our derivation of the signal sample redshift distribution is based on three assumptions: the IceCube Collaboration accurately reports the probability that an observed neutrino is astrophysical (i.e., not created by cosmic rays interacting in the atmosphere), CC SNe are the sole component of the teraelectronvolt to petaelectronvolt energy neutrino flux, and CC SN redshifts are distributed according to the cosmic massive star formation rate (Madau & Dickinson 2014). We elaborate on our first assumption in Section 3.1. The second assumption is relaxed in Section 6 when we assess the necessities of a sustained optical follow-up campaign for different fractions of CC SN contribution to the IceCube flux. Lastly, the third assumption is physically motivated because stars with mass greater than $\sim 8 M_{\odot}$ are expected to end in CC SNe (Burrows et al. 1995).

Based on the final assumption, we obtain the expected redshift distribution of associated CC SNe that we detect in our follow-up observations using the following equation for the cumulative neutrino intensity as a function of redshift:

$$\begin{aligned} & \frac{dN_{\nu}(E_{\nu})}{dE_{\nu}d\Omega dt_{\text{obs}}dA} \\ &= \int_0^{z_{\text{max}}} \frac{dV}{dzd\Omega} \frac{1}{4\pi D_L^2} \frac{dN_{\nu}(E_{\nu}(1+z))}{dE_{\nu}} \frac{1}{1+z} \mathcal{R}(z)\varepsilon(z) dz. \end{aligned} \quad (1)$$

In Equation (1), $dV/(dzd\Omega)$ is the comoving volume element, $1/(4\pi D_L^2)$ is a division by the surface area of a sphere with radius equal to the luminosity distance, $dN_{\nu}(E_{\nu}(1+z))/dE_{\nu}$ is the predicted number of observed neutrinos with energy E_{ν} from a CC SN at a given redshift, $1/(1+z)$ is the general relativistic time-dilation factor, $\mathcal{R}(z)$ is the formation rate for stars that will become CC SNe at a given redshift, and $\varepsilon(z)$ is the optical detection efficiency for associated CC SNe. Integrating from $z = 0$ to $z = z_{\text{max}}$ gives the cumulative neutrino intensity from CC SNe that explode up to redshift z_{max} . For this calculation and for the simulations used in Section 4, we adopt a flat Λ CDM cosmology with Hubble constant $H_0 = 67.77 \text{ km s}^{-1} \text{ Mpc}^{-1}$ following the type

Table 1

Properties of the Two Southern-sky, High-energy IceCube Alerts Observable from CTIO from 2017 August through 2018 January, and DECam Observing Cadences and Conditions

<i>IceCube Neutrino Alerts</i>		
Name	IC170922A	IC171106A
Date	2017 Sep 22	2017 Nov 6
Time (UTC)	20:54:30.43	18:39:39.21
Neutrino energy (TeV)	120.0	230.0
R.A. (deg)	$77.43^{+0.95}_{-0.65}$	$340.25^{+0.70}_{-0.25}$
Decl. (deg)	$+5.72^{+0.70}_{-0.50}$	$+7.31^{+0.35}_{-0.25}$
Containment region	0.97	0.57
Area (90% C.L.) (deg ²)		
signalness ^a	0.56507	0.74593
<i>Blanco/DECam Follow-Ups</i>		
Observing nights	1, 3, 10, 20, 21	1, 2, 4, 10, 16
after alert		
First night—alert	10.72	7.22
time difference (hours)		
Filters	<i>g r i</i> ^b	<i>g r i z</i> ^c
Exposure time (s)	2×150	2×150
per band per epoch		
Effective DECam	3.12	2.71
FoV area (deg ²)		
5σ Mag limit (<i>g, r, i</i>)	23.6, 23.7, 23.3	23.4, 23.5, 23.1
Average air mass	1.24	1.26

Notes.

^a “Signalness” is Described in Section 3.1.

^b Only *gr* were used on the final observing night.

^c *gri* for all nights except the final night, which was *riz*.

Ia SNe measurement made by the Dark Energy Survey (Macaulay et al. 2019). We also take fractions of the universe’s energy density made up by matter and dark energy to be $\Omega_m = 0.298$ and $\Omega_\Lambda = 0.702$, respectively, following the combined probe measurements of the Abbott et al. (2018).

3. Observations and Data

In this section, we provide background on the instruments used in this analysis and detail the relevant observations. We summarize this section in Table 1.

3.1. IceCube Real-time Neutrino Alerts

IceCube is a cubic-kilometer-scale neutrino detector located at the geographic South Pole and built into the Antarctic ice at depths ranging from 1450 to 2450 m (Aartsen et al. 2017b). Incident neutrinos are detected indirectly through Cerenkov radiation emitted by secondary charged particles produced in the interaction of a neutrino with a nucleus of the ice. Photomultipliers in 5160 optical modules sense the Cerenkov light. Events detected by IceCube are classified as “shower” events or “track” events. Showers are produced in charged-current interactions of electron and tau neutrinos and in neutral-current interactions of all neutrino flavors. A shower of secondary particles with a few meters of extension is produced, which is small compared to the distance between the optical modules. Therefore, the Cerenkov light produced by the shower particles appears almost spherical. Such events can be reconstructed with an angular resolution of the incoming neutrino on the order of ~ 15 deg. Tracks are produced by

charged-current interactions of muon neutrinos in or close to the detector, which produce a muon that travels along a long linear path through the ice, providing a good lever arm for the angular reconstruction. Specifically, for track neutrino events with energies above 100 TeV, IceCube achieves median angular resolutions for high-energy starting events (HESE) and extremely high energy events (EHE) of 0.4–1.6 deg and < 1.0 deg, respectively (Aartsen et al. 2014, 2017a).

In an effort to locate the sources of these neutrinos and to facilitate follow-up studies, the IceCube Collaboration has created a real-time alert system for events of likely astrophysical origin (Aartsen et al. 2017a). The system has a median latency of 33 s in which neutrino events are processed and reconstructed. Within three minutes, alerts are published to streams such as the Astrophysical Multimessenger Observatory Network (AMON; Smith et al. 2013; Keivani et al. 2017) and the Gamma-ray Coordination Network (GCN; Barthelmy et al. 1998). Alerts are accompanied by an estimate of the probability that the neutrino is of astrophysical origin, referred to as the “signalness.” The signalness describes how likely the event is of astrophysical origin relative to the total atmospheric background rate and is a function of the neutrino energy and the zenith angle. For more information on the calculation of the signalness, refer to the discussion in Aartsen et al. (2017a).

On 2017 September 22, IceCube detected a singular high-energy neutrino. Another singular high-energy neutrino was detected on 2017 November 6. Both events had good angular resolution and are likely to be of astrophysical origin. The details of the AMON alerts are presented in the top portion of Table 1. Both alerts were track-type singular neutrinos with energies on the 100–200 TeV scale. These alerts featured signalness scores of ~ 0.57 and ~ 0.75 and 90% confidence level containment region areas smaller than the FoV of DECam. The high energies and signalness scores suggest an astrophysical origin of the events and motivate the search for an optical counterpart in the form of CC SNe.

Of the 31 alerts issued thus far by the IceCube Collaboration, 21 have occurred after the start of this analysis. Of the 21 possible alerts, 16 were either deemed unobservable based on atmospheric, moon, or Sun conditions, or were retracted by the IceCube Collaboration. The two alerts presented here are two of only five alerts that have been observable from the location of the Blanco Telescope in Chile. The additional alerts (IC181023A, IC190331A, and IC190503A) were observed and will be discussed in a future work.

3.2. DECam Imaging Follow-up

The Dark Energy Camera (Flaugher et al. 2015) is a 570-megapixel optical imager mounted on the 4 m Blanco Telescope at Cerro Tololo Inter-American Observatory (CTIO) in Chile. Blanco/DECam’s location, FoV (~ 3 deg²), and deep imaging capabilities make it the only southern hemisphere imager with a wide FoV matched to the IceCube angular resolution and a large enough aperture to efficiently detect explosive optical transients at the redshifts relevant for proposed neutrino sources.

The Dark Energy Survey is a wide-field optical survey (expected to reach a 10σ depth for point sources of $grizY = 25.2, 24.8, 24.0, 23.4, 21.7$ mag over 5000 deg²) with 577 full DECam observing nights (Mohr et al. 2012). Operating within a large survey program is ideal for our follow-up study because there is no need to interrupt

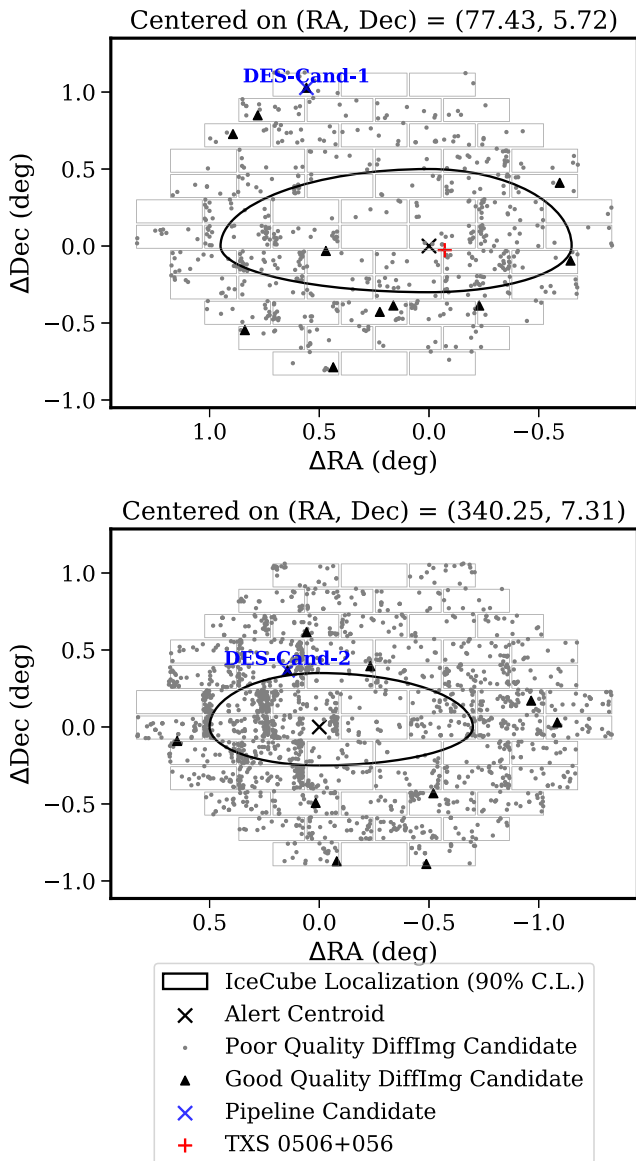


Figure 1. DECam fields of view for the IC170922A follow-up (top) and for the IC171106A follow-up (bottom) showing difference imaging products, the containment region for the neutrino direction at the 90% confidence level, and the candidates selected by our Neutrino Candidate Identification Pipeline (NCIP). The location of TXS 0506+056 is also shown for reference.

community observers, and the interruptions are short (20 minutes). Specifically, we use triggered target-of-opportunity observations to promptly respond to IceCube alerts. Our observing strategy was to dedicate about one month to characterize the rise and peak of potentially associated CC SNe for each alert. During the one-month observing period, we took observations roughly every five to six nights depending on atmospheric and moon conditions. As well, we added an additional observing night to the start of the follow-up to look for rapidly evolving optical transients. Observations consisted of two 150 s exposures in each of the *gri* optical bands, and exposures within the same band were stacked to reduce noise and increase imaging depth. For the IC170922A follow-up, we also adjusted the pointing of the telescope by 0.01 deg in both R.A. and decl. between exposures of the same band to cover areas of the sky that mapped to gaps between adjacent CCDs,

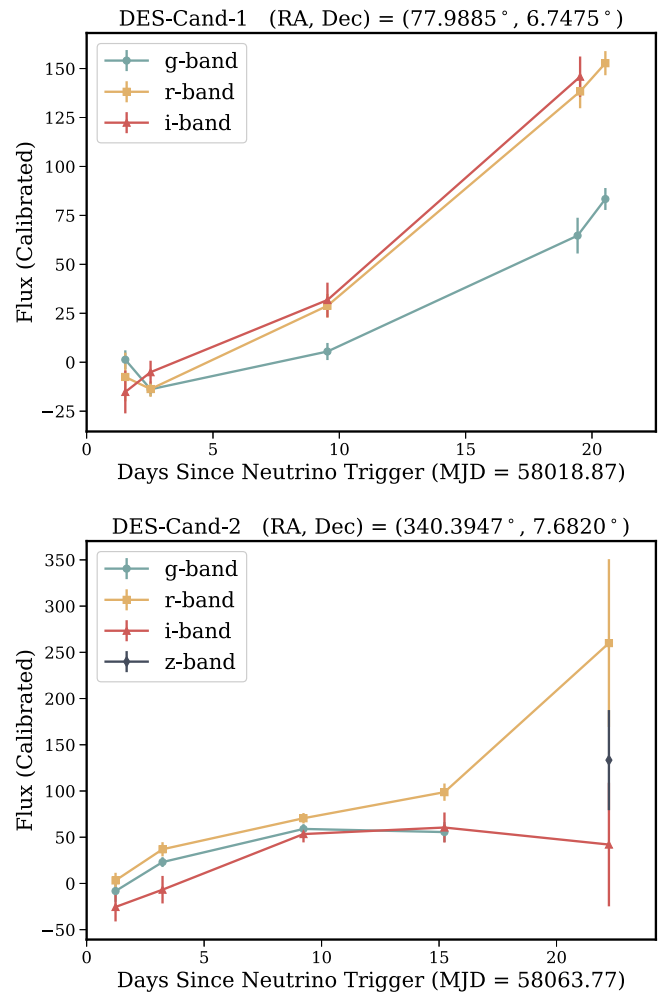


Figure 2. Top: light curves in *gri* for DES-Cand-1, one of the difference imaging products selected by NCIP in the IC170922A follow-up. Bottom: light curves in *griz* for DES-Cand-2, the candidate from the IC171106A follow-up.

leading to a slightly larger effective DECam FoV area in Table 1.

The DECam observations were processed by the DES Difference Imaging Pipeline (Kessler et al. 2015, DiffImg), which subtracts template images from the observations and produces catalog-level photometric fluxes in each band for all detected transients in the FoV. For this analysis, since our observations did not overlap with the DES footprint where template images would be readily available, we use the first-night images as templates. Observations are also run through *autoscan* (Goldstein et al. 2015), which identifies potential image artifacts and poor image subtractions. This process injects fake artifacts into the images to train the algorithm to remove artifacts that may be present in the images. The probability that a DiffImg candidate is a real astrophysical object as opposed to an artifact is characterized by the *autoscan* machine learning (ML) score. This score is utilized in Section 4. From the DiffImg outputs, objects that are likely CC SNe and temporally coincident with the neutrino alert based on light curve properties are selected by an automated neutrino source candidate identification pipeline described in Section 4. The DiffImg products and pipeline candidates for both IC170922A and IC171106A are shown in Figure 1. The light curves of the pipeline candidates are shown in Figure 2.

3.2.1. DECam Observations of TXS 0506+056

One of the two neutrino alerts considered in this work, IC170922A, is likely to be associated with the flaring gamma-ray blazar TXS 0506+056. The link is based on an analysis of nearly a decade of *Fermi*-LAT observations of gamma-ray blazars, as well as triggered observations of TXS 0506+056 during its flaring state covering the full electromagnetic spectrum (IceCube Collaboration et al. 2018). In addition, a search in archival IceCube data at the position of TXS 0506+056 revealed an excess of lower energy neutrinos during a 158 day period in 2014 and 2015 with a significance of 3.5σ (IceCube Collaboration 2018b).

We mark the location of TXS 0506+056 within the DECam FoV in Figure 1. TXS 0506+056 was bright in optical bands around the time of the neutrino alert, reaching $V \sim 14$ mag (IceCube Collaboration et al. 2018). Our choice of 150 s exposure times was optimized to search for faint optical transients at ~ 23 mag, and as a result, TXS 0506+056 is saturated in the DECam images because of the finite dynamic range of the camera. Optical imaging, spectroscopy, and polarimetry for the event were obtained from a combination of ASAS-SN, Kanata/HONIR, Kiso/KWFC, Liverpool Telescope, and Subaru/FOCAS (IceCube Collaboration et al. 2018).

In the discussion that follows, we quantify the sensitivity of DECam to explosive optical transients independent of the probable association between IC170922A and TXS 0506+056.

4. Sensitivity Analysis Using Simulations

As evidenced by Figure 1, *DiffImg* recovers many moving objects, variable objects, and transients within a typical neutrino localization region including asteroids, active galactic nuclei (AGNs), and background SNe. The background SNe population is composed of type Ia SNe, CC SNe exploding before the neutrino alert but persisting into the observing window, CC SNe exploding near the time of the neutrino alert, and CC SNe exploding after the alert but becoming bright enough to be optically detectable before the observing window has concluded. The removal of unassociated transients from our observations is critical for isolating potential neutrino source candidates. We therefore develop selection criteria to remove CC SNe exploding before or much later than the neutrino trigger and type Ia SNe altogether. The selection criteria applied to the *DiffImg* output are collectively named the Neutrino Candidate Identification Pipeline (NCIP). The following analysis demonstrates the extent to which these unassociated transients can be removed from DECam observations while maintaining a high detection efficiency for the potentially associated CC SN.

4.1. Simulations and Candidate Selection

Selecting CC SNe associated with IceCube neutrino alerts requires extrapolating the explosion time of the SN from its light curve. To model the rise times of SNe, we employ the SuperNova ANALysis software suite (SNANA; Kessler et al. 2009), which enables us to simulate SN light curves based on our observing cadence. Based on SNANA-simulated SN light curves for our observations, we develop selection criteria to filter out unassociated SNe. Then by applying the selection criteria to the same simulations, we determine the detection

efficiency for an associated CC SN and the expected number of unassociated SNe found by NCIP for each follow-up.

We simulated SNe light curves for 500 DECam FoVs for each follow-up. The background population of simulated light curves consists of both type Ia and CC SNe that reach peak brightness in a range of MJDs extending from 30 nights before the observing window to 100 nights after the observing window has concluded. For the simulated type Ia SNe, we use templates from Guy et al. (2010) and rates from Dilday et al. (2008), and for the simulated CC SNe we use templates from Kessler et al. (2010) and rates from Bernstein et al. (2012). We do not include asteroids or AGNs in the background sample because those models are not available within SNANA, though it has been shown that they can be effectively removed with additional selection criteria (Bailey et al. 2007). The simulated signal population consists of only CC SNe with an explosion time set to be the date of the IceCube neutrino alert. Since explosion times are not observed, CC SNe models are more tightly constrained near peak brightness than during the rising phases, and we therefore use the flux relative to its peak value as a proxy for when the explosion began. Within SNANA, we define the explosion time to be the earliest MJD for which the flux in any band reaches 1% of the peak flux in the rest frame of the SN. To construct the signal sample, CC SN light curves are scanned for the MJD exhibiting a rise in flux above the 1% peak flux level, and then shifted in time so that the MJD aligns with the desired explosion time. By setting the neutrino trigger to the date of the start of the explosion, we are only considering prompt neutrino emission in this analysis, rather than neutrino emission that may occur during later stages of the collapse. Both sets of simulations account for the measured point-spread function, zero point, and sky noise in each exposure to yield a light curve quality that is representative of the actual DECam follow-up observations. The simulations do not account for uncertainty in the CC SN luminosity function, which is currently approximated using a Gaussian distribution with a mean and standard deviation determined from observed SN luminosity (Li et al. 2011).

The process of background removal consists of a series of selection criteria applied to the simulated light curves. We list the criteria here and discuss the motivation for each cut in the remainder of this section:

1. *Quality Cut.* Light curves must have detections on two separate nights, irrespective of the band of the detection. If a light curve passes this cut, we refer to it as “optically detectable.”
2. *Rising Cut.* Light curves must not have a detection on the first post-template night following the trigger, or if there is a detection, there must be an increase in flux of at least one magnitude in at least one band over the first two post-template nights.
3. *Phase Cut.* The peak MJDs predicted by the type Ibc and type II templates fit to the light curve must be at least six nights and 16 nights after the trigger, respectively.
4. *Classify Cut.* Light curves must be classified as a CC SN by our Random Forest Classifier.

Quality. The quality cut is designed to guarantee DECam detectability from photometric data quality. For this cut and the rising cut, we define a “detection” in a given band and epoch to mean the photometric data has the following three properties: (1) *DiffImg* finds the object and does not mark it as a bad

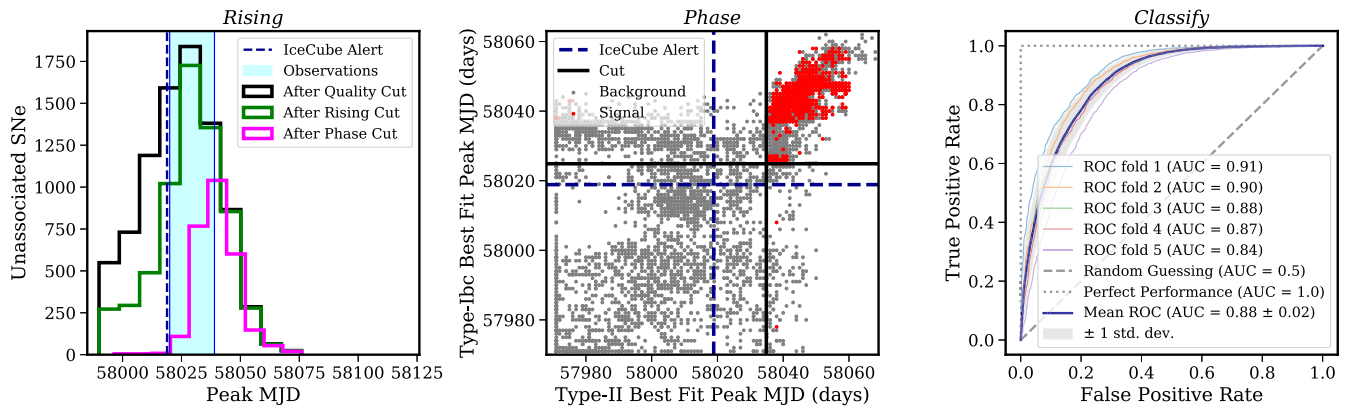


Figure 3. Selection criteria motivation and effectiveness based on simulations of the IC170922A follow-up. Left: distribution of peak MJD values from the background sample after successive cuts. Center: best-fit peak MJD values from type II and type Ibc template fits with cuts displayed. Right: receiver operating characteristic (ROC) curves of our Random Forest Classifier implemented on each fold of the training sample during a fivefold cross validation. Each curve has an associated area under curve (AUC) to characterize the performance of the classifier.

subtraction; (2) the ML score is larger than 0.7, meaning observation was determined to have good image quality and is unlikely to be an artifact; and (3) the signal-to-noise ratio is larger than 10. The quality cut removes events that are photometrically of too poor quality to claim association with the neutrino by ensuring that the event is observable with DECam. In the DECam FoV, we expect 17.5 ± 0.3 SNe and observe 11 objects for IC170922A, and for IC171106A we expect 10.0 ± 0.3 SNe and observe 10 objects. The under-fluctuation for IC170922A is mediated by the application of further cuts.

Rising. The rising cut is designed to select light curves of recently exploded objects by removing SNe that reach peak brightness before the neutrino trigger. The effectiveness of the rising cut is shown in the left panel of Figure 3. For the two follow-ups presented here, the first observing night was used to make template images. Therefore, “post-template” nights refer to all nights after the first night. In future follow-ups, if it is not possible to observe the field right away, or if template images already exist, this criterion will need to be reformulated. After the rising cut, we expect 13.1 ± 0.3 SNe in the DECam FoV for IC170922A and observe 10 objects, and for IC171106A we expect 7.3 ± 0.3 SNe and observe eight objects.

Phase. The most differentiating features between the signal and background populations that pass the first level of cuts are the type of SN and where in time the SN exploded relative to the neutrino trigger, which we refer to as the *phase* of the light curve. To exploit these features, we fit all light curves using the SNANA implementation of the Photometric SuperNova IDentification tool (Sako et al. 2011, PSNID), which offers not only best-fit phase information but also fit probabilities and χ^2 values for the type Ia, type Ibc, and type II templates fit to each light curve (henceforth χ_{Ia}^2 , χ_{Ibc}^2 , and χ_{II}^2). The phase cut is designed to remove light curves that exploded before the trigger and are still rising during the observing window. The cutoffs of six and 16 nights were empirically derived from analyzing simulations. The motivation for these values is displayed in the center panel of Figure 3, and the performance of the phase cut is also shown in the left panel of the same figure. After imposing the phase cut, we expect 5.6 ± 0.2 SNe in the DECam FoV for IC170922A and observe two objects, and for IC171106A we expect 2.74 ± 0.17 SNe and observe two objects.

Classify. Since PSNID was designed to make classifications with the goal of maximizing type Ia SNe purity, we opted to supplement the information used to make classifications with features that are tailored to the problem of selecting CC SNe. Specifically, we found that by including features representative of the probability a light curve was a CC SN, we were able to increase the fraction of known CC SNe classified as CC SNe (CC completeness) while simultaneously reducing the fraction of known type Ia SNe classified as CC SNe (Ia false-positive rate). PSNID returns χ^2 values for light curve fits to type Ia (χ_{Ia}^2), type Ibc (χ_{Ibc}^2), and type II (χ_{II}^2) templates. Based on this information, we define the normalized Ia and CC χ^2 values $\bar{\chi}_{\text{Ia}}^2$ and $1 - \bar{\chi}_{\text{CC}}^2$, where

$$\bar{\chi}_{\text{Ia}}^2 = \frac{\chi_{\text{Ia}}^2}{\chi_{\text{Ia}}^2 + \chi_{\text{Ibc}}^2 + \chi_{\text{II}}^2} \quad \text{and} \quad (2)$$

$$\bar{\chi}_{\text{CC}}^2 = \frac{\min(\chi_{\text{Ibc}}^2, \chi_{\text{II}}^2)}{\chi_{\text{Ia}}^2 + \chi_{\text{Ibc}}^2 + \chi_{\text{II}}^2}. \quad (3)$$

Both of the features range from zero to one, and they are expected to be closer to zero for a type Ia SN while closer to one for a CC SN. Using these features, we reclassified the sample using a Random Forest Classifier (Breiman 2001) implemented with `Sci-Kit Learn` (Pedregosa et al. 2011). To construct the classifier, we first used principal component analysis (PCA; Tipping & Bishop 1999) with eight components to project light curve fit information to the space of largest variance, and then employed an ensemble of 1000 decision-tree classifiers with a restriction of 50 for the maximum tree depth. The number of principal components, number of decision trees, and depth restriction on the decision trees were determined via an extensive search of the hyperparameter space using a separate validation data set.

The classifier was trained using a SNANA-simulated sample of CC light curves passing the quality, rising, and phase cuts that had an explosion time set to the neutrino trigger and a low redshift ($z < 0.3$) as the target class. The background class was composed of CC and type Ia light curves determined that passed the quality, rising, and phase cuts with no set restriction on the true explosion time of the SNe. We also include spectroscopically confirmed CC SNe and Ia SNe from the DES

Table 2
Application of the Candidate Selection Pipeline to Simulations and Data for IC170922A and IC171106A

IC170922A Follow-up								
Sample	Signal Efficiency		Signal Efficiency		Background Events ^a in IC90		Data ^b	Data ^b
	All SNe ^a		Optically Detectable SNe ^a				in FoV	in IC90
Cut	$z < 0.3$	$z > 0.3$	$z < 0.3$	$z > 0.3$	$z < 0.3$	$z > 0.3$
Total	1.0000 $_{-0.0001}$	1.00000 $_{-0.00001}$	9.26 ± 0.14	414.2 ± 0.9	617	240
Quality	0.199 $^{+0.004}_{-0.004}$	2.47 $^{+0.16}_{-0.15} \times 10^{-3}$	1.0000 $_{-0.0006}$	1.000 $_{-0.005}$	1.48 ± 0.05	3.96 ± 0.09	11	2
Rising	0.198 $^{+0.004}_{-0.004}$	2.47 $^{+0.15}_{-0.15} \times 10^{-3}$	0.9984 $^{+0.0007}_{-0.0011}$	1.000 $_{-0.005}$	1.00 ± 0.04	3.07 ± 0.08	10	2
Phase	0.179 $^{+0.004}_{-0.004}$	2.47 $^{+0.15}_{-0.15} \times 10^{-3}$	0.9964 $^{+0.0012}_{-0.0015}$	1.000 $_{-0.005}$	0.51 ± 0.03	1.25 ± 0.05	2	0
Classify	0.121 $^{+0.003}_{-0.003}$	1.26 $^{+0.11}_{-0.11} \times 10^{-3}$	0.608 $^{+0.011}_{-0.011}$	0.51 $^{+0.03}_{-0.03}$	0.116 ± 0.015	0.113 ± 0.015	1	0

IC171106A Follow-up								
Sample	Signal Efficiency		Signal Efficiency		Background Events ^a in IC90		Data ^b	Data ^b
	All SNe ^a		Optically Detectable SNe ^a				in FoV	in IC90
Cut	$z > 0.3$	$z > 0.3$	$z < 0.3$	$z > 0.3$	$z < 0.3$	$z > 0.3$
Total	1.0000 $_{-0.0001}$	1.00000 $_{-0.00001}$	5.13 ± 0.10	236.4 ± 0.7	1868	646
Quality	0.134 $^{+0.003}_{-0.003}$	7.1 $^{+0.9}_{-0.8} \times 10^{-4}$	1.0000 $_{-0.0008}$	1.000 $_{-0.016}$	0.65 ± 0.04	1.46 ± 0.05	10	0
Rising	0.134 $^{+0.003}_{-0.003}$	7.1 $^{+0.9}_{-0.8} \times 10^{-4}$	0.9978 $^{+0.0010}_{-0.0016}$	1.000 $_{-0.016}$	0.43 ± 0.03	1.11 ± 0.05	8	0
Phase	0.130 $^{+0.003}_{-0.003}$	7.1 $^{+0.9}_{-0.8} \times 10^{-4}$	0.970 $^{+0.004}_{-0.005}$	0.986 $^{+0.010}_{-0.02}$	0.187 ± 0.019	0.39 ± 0.03	2	0
Classify	0.095 $^{+0.003}_{-0.003}$	3.3 $^{+0.4}_{-0.4} \times 10^{-4}$	0.713 $^{+0.012}_{-0.012}$	0.46 $^{+0.06}_{-0.06}$	0.047 ± 0.010	0.020 ± 0.006	1	0

Notes. The term “optically detectable” is equivalent to the light curve passing the quality cut. Background event values have a statistical uncertainty of $\pm \sqrt{N}/500$ on the mean number of events generated, corresponding to the number of DECam FoVs simulated. The uncertainties reported for the signal efficiencies give a 68% confidence interval. The numbers of background events reported are scaled to reflect just the events within the IceCube 90% CL containment region. The data in the total row are not expected to match the simulations because they can contain non-SNe transients or bad image subtractions that are removed by the quality cut.

^a Results presented are based on SNANA simulations.

^b Results presented are the number of candidates remaining from DECam observations.

3 Year SNe sample (Macaulay et al. 2019) in the training set signal and background samples, respectively. The ratio of simulated SNe to real SNe in the training set was found to strongly correlate to classifier accuracy, and we determined the optimum ratio for each follow-up using independent validation sets. We find that classification accuracy is optimized for both simulated and real SNe when 36% (40%) of the training set is simulated for IC170922A (IC171106A), and the determination of these ratios is shown in Figure 4. The dependence in classification accuracy on the inclusion of real SNe is likely due to the fact that the real SNe were observed under better conditions than our follow-ups. Since our classifier uses best-fit properties to make predictions, it is sensitive to how well the light curve fitting reflects the true properties of the explosion, so the better observing conditions of the real SNe could add new classification information that a simulated training set lacked.

In the process of training, we used stratified fivefold cross validation to limit overfitting. This procedure trains on four-fifths of the training data, tests on the remaining one-fifth, and then repeats the process so that each fifth of the training data is used once for testing; the purpose is to introduce small variations in the training set so that the classifier does not effectively memorize the training set. The classifier operates at 83.7% purity, 68.1% completeness, and with a 7.3% false-positive rate on the training set, and at 81.8% purity, 66.7% completeness, and with a 8.1% false-positive rate on the testing set. The similarity of the performance of the classifier on familiar and unseen data is a good indicator that the classification is not suffering from overfitting and will be able to generalize to other data sets. An ROC curve for our classifier

is displayed in the right panel of Figure 3 and shows the classifier operating with a mean area under curve (AUC) of 0.88. The standard deviation of the AUC over the five folds of the training data is 0.02, indicating classifications are relatively insensitive to the representation of exact members of the training set. After this final cut, we expect 0.74 ± 0.07 SNe in the DECam FoV for IC170922A and observe one object, and for IC171106A we expect 0.32 ± 0.06 SNe and observe one object. These two remaining objects are our candidates from these first two follow-up efforts.

4.2. Sensitivity Results

We applied the selection criteria to our SNANA simulations of the signal and background samples. For the signal samples, we report the fraction of events passing each successive cut, as well as the fraction of optically detectable events passing each successive cut. These fractions are multiplied by the CC SN rate to determine the expected number of signal-like events per IceCube alert as a function of redshift and scaled to the IceCube 90% confidence level containment region (IC90). The number of background events passing each cut was normalized based on the number of FoVs generated to accurately reflect the expected number of background-like events per follow-up. These results are presented for each of the two events in Table 2.

For events with observing conditions of quality similar to the IC170922A follow-up, we expect to detect roughly 12.1% of nearby ($z < 0.3$), neutrino-emitting CC SNe using DECam and NCIP, while limiting the background to 0.23 unassociated SNe up to redshift $z = 1$ within IC90. For the events similar to the IC171106A follow-up observations, we expect to detect 9.5%

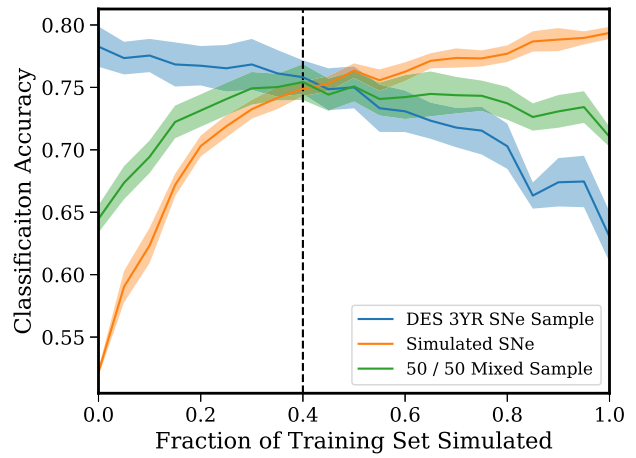
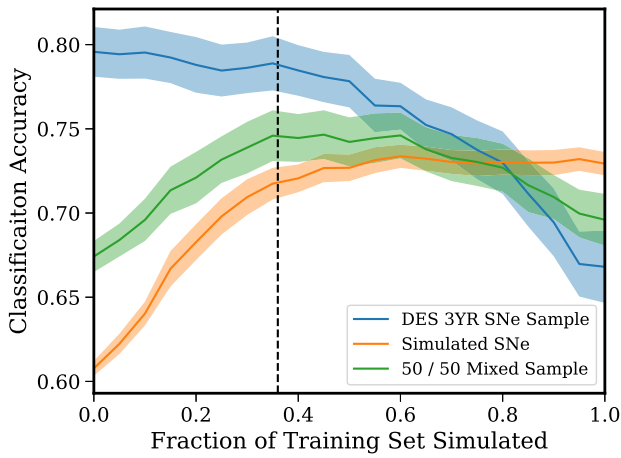


Figure 4. Classifier accuracy for real SNe, simulated SNe, and a mixed sample parameterized by the fraction of the training set composed of simulated SNe. The optimum fraction chosen for training is shown by the black dashed line. Left: based on the IC170922A follow-up. Right: based on the IC171106A follow-up.

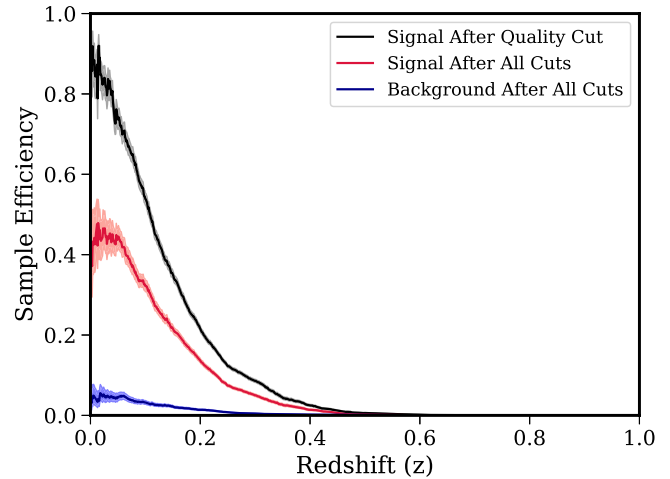
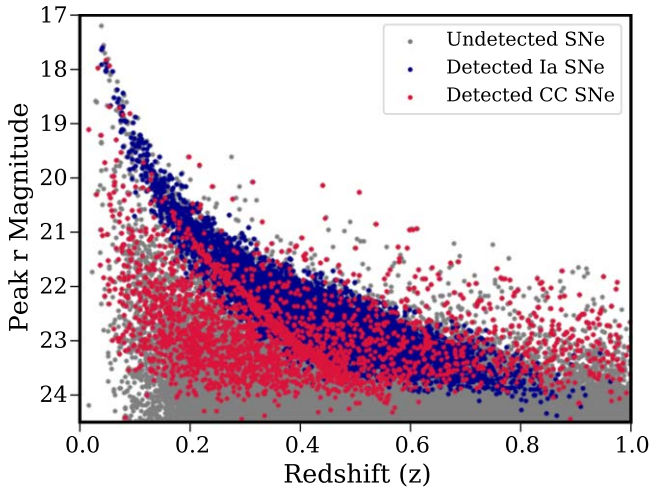


Figure 6. Detection efficiency parameterized by redshift for the signal and background populations based on simulations of the IC170922A follow-up observations. The solid black line illustrates the fraction of CC SNe that would be detectable by DECam, while the solid red line shows the fraction of all CC SNe that pass our selection criteria. The shaded error regions give a 68% confidence interval.

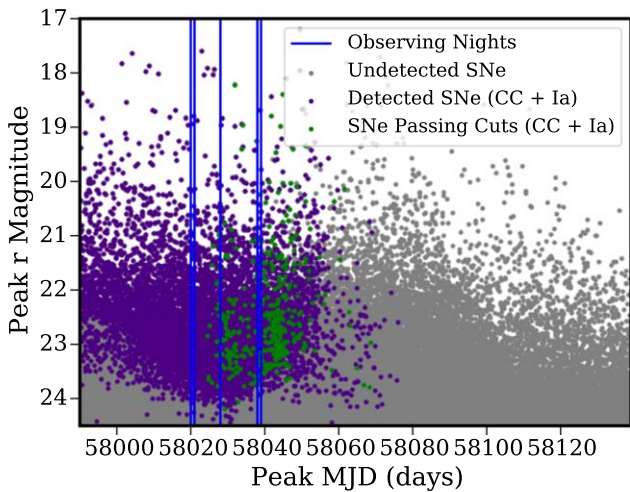


Figure 5. Remaining SN background events for the IC170922A simulations. Top: peak r -band magnitude versus the MJD of largest flux with reference MJDs of the IceCube alert and the DECam observing nights. Bottom: peak r -band magnitude versus redshift. Both figures display 500 times as many events as would be expected in a single DECam field of view.

of nearby signal events and 0.067 background events within IC90 per follow-up. The low signal detection efficiency is a result of the faintness of CC SNe and the magnitude limit of

DECam, rather than the strictness of our selection criteria, evidenced by roughly 90% of optically detectable, low-redshift signal events passing all cuts across both events. The remaining SNe background sample’s magnitude, temporal, and redshift distributions are displayed in Figure 5.

Next, we consider the signal detection efficiency and number of remaining background events per set of follow-up observations as functions of redshift in order to calculate the maximum redshift to which we will be able to detect the potential CC SN counterpart of an IceCube alert. These relationships are shown for the IC170922A follow-up in Figure 6. Based on Figure 6, the fraction of signal sample events remaining after all cuts quickly diminishes as redshift increases; however, this behavior is largely a result of the low optical detectability of high-redshift CC SNe.

The distribution of remaining background events per set of follow-up observations based on the observing conditions of the IC170922A follow-up is shown as a function of redshift in Figure 7. We note that the type Ia SNe background has been

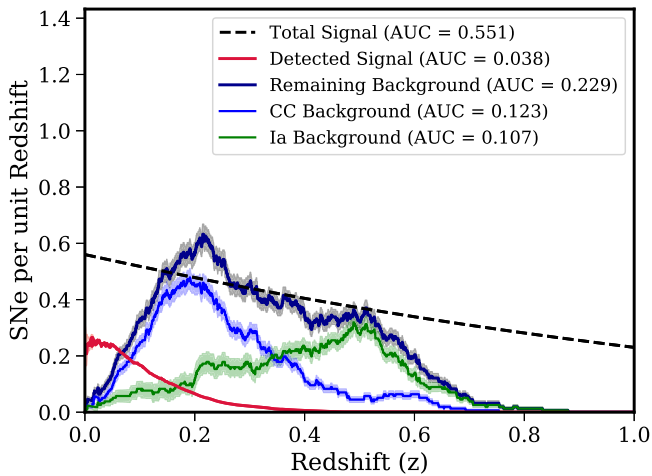


Figure 7. Predicted number of events versus redshift based on simulations of the IC170922A follow-up after the selection criteria have been applied. Shaded error regions give a 68% confidence interval for the signal curve and a standard Poisson statistical uncertainty for the background curves. The AUC shows the cumulative number of expected events in the solid angle of the IceCube 90% containment region.

suppressed in the redshift range of highest sensitivity (approximately $z < 0.2$). Therefore, only events that are similar to the signal population in both SN type and phase remain in the final SNe background population. The background sample of this analysis was normalized within *SNANA* such that the number of events generated was equal to the expected number of SNe within a DECam FoV. The signal sample is normalized to one CC SNe, since only one or zero signal CC SNe is possible per follow-up. The redshift distribution is derived by folding the detection efficiency as a function of redshift with the cosmic star formation rate as described in Section 2. We also multiply the signal distribution by the IceCube signalness value, which is the probability that the neutrino has an astrophysical origin.

From the signal and background redshift distributions, we integrate over all redshifts to obtain the total number of expected signal and background events for a given follow-up. These numbers are displayed on Figure 7 as the AUC values and become important when redshift information for pipeline candidates is unavailable, requiring us to account for all events along the line of sight. Next, we compare the expected number of detected CC SNe associated with the IceCube alert to the number of unassociated SNe expected to pass our selection criteria in a single follow-up observation. Figure 7 displays this comparison for the IC170922A follow-up. The signal clearly dominates the background at low redshifts, and the cumulative number of signal events dominates the cumulative number of background events until roughly $z = 0.1$. Beyond this redshift, uncertainties in the modeling of SN rise times weaken the effect of the timing-based cuts (rising and phase) on reducing the background. Additionally, as the redshift increases, CC SNe exploding at the time of the neutrino alert quickly become too faint to detect. Together, both of these effects lead to background domination at high redshifts.

5. Results of DECam Observations

We apply our candidate selection pipeline to the difference imaging results for the IC170922A and IC171106A follow-up efforts. We apply two additional selection criteria to our

Table 3
NCIP Candidates for Each Follow-up and Results of Maximum-likelihood Analysis

<i>IC170922A Follow-Up Candidates</i>				
Name	R.A. (deg)	Decl. (deg)	z	Prob.
DES-Cand-1	77.9885	6.7475	...	0.0
Test statistic:				0.0
p Value:				>0.999
<i>IC171106A Follow-Up Candidates</i>				
Name	R.A. (deg)	Decl. (deg)	z	Prob.
DES-Cand-2	340.3947	7.6820	0.31	0.1055
Test statistic:				0.0558
p Value:				0.0250
Global test statistic:				0.0143
Global p value:				0.0930

Note. The uncertainties on the R.A. and decl. from *DiffImg* are negligible, and the uncertainty on the redshift of DES-Cand-2 is ± 0.02 . The rightmost column is the probability that the candidate is associated with the neutrino based on the expected signal and background events in the spatial bin of the candidate. The details of the likelihood analysis are presented in Appendix A. The p values refer to the hypothesis test of CC SNe contributing to the IceCube neutrino flux as a population, rather than the association between the neutrino and candidate.

observations for effects that were not simulated. First, we exclude candidates that move $0''.1$ or more between observations to exclude asteroids. This cut did not remove anything that was not already removed by the quality cut. Second, we perform a catalog search of all pipeline candidates and exclude objects with an angular separation less than $0''.4$ from a known AGN or quasar. This criterion removed one candidate from each follow-up. For each DECam follow-up, we display the number of potential candidates remaining after each successive cut in the rightmost column of Table 2. One difference imaging candidate passed all cuts from IC170922A (DES-Cand-1), and one candidate passed all cuts for IC171106A (DES-Cand-2).

For the candidates found by NCIP, the coordinates and IceCube 90% confidence intervals are shown in Figure 1, the light curves are shown in Figure 2, and image stamps are shown in Figures 8 and 9. As shown in Table 2, the number of SNe expected to pass our selection criteria per follow-up is between zero and one, so it is likely that these candidates are SNe. The light curves display a clear rise, and the image cutouts show a transient object within a host galaxy. A photometric redshift estimate was found for DES-Cand-2 using the methods of Soares-Santos et al. (2019), which employed a machine learning approach described in Sadeh et al. (2016). This approach requires exposures in at least four bands, so we were not able to apply it to DES-Cand-1.

For the candidates selected by NCIP, we determined the probability that each candidate was associated with the neutrino source based on the numbers of expected signal and background events in the spatial bins of the candidate. This process is detailed in Appendix A. We also used the candidates to test the hypothesis that CC SNe contribute to the total IceCube neutrino flux. The significance levels of the hypothesis tests and the individual candidate probabilities are displayed in Table 3. Individually, the detected candidates are consistent with the expected backgrounds for their respective alerts

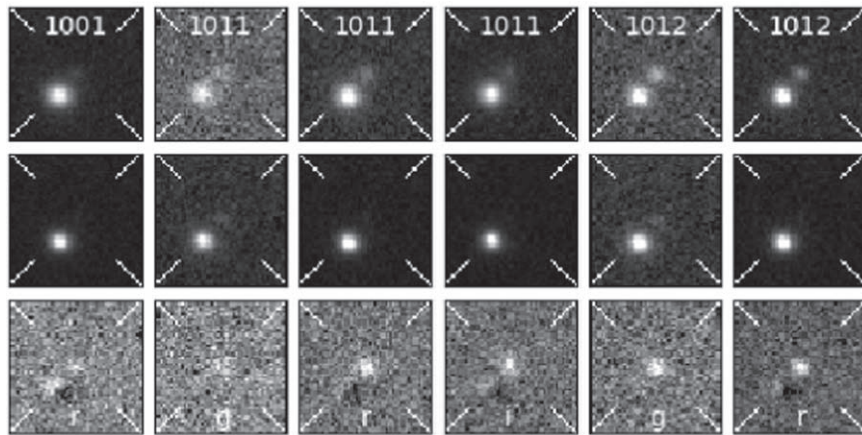


Figure 8. Image stamps for DES-Cand-1. The top row is the search image, the middle row is the template, and the bottom row is the difference image. Filters are shown at the bottom of each column, and dates are given in MMDD format at the top of each column.

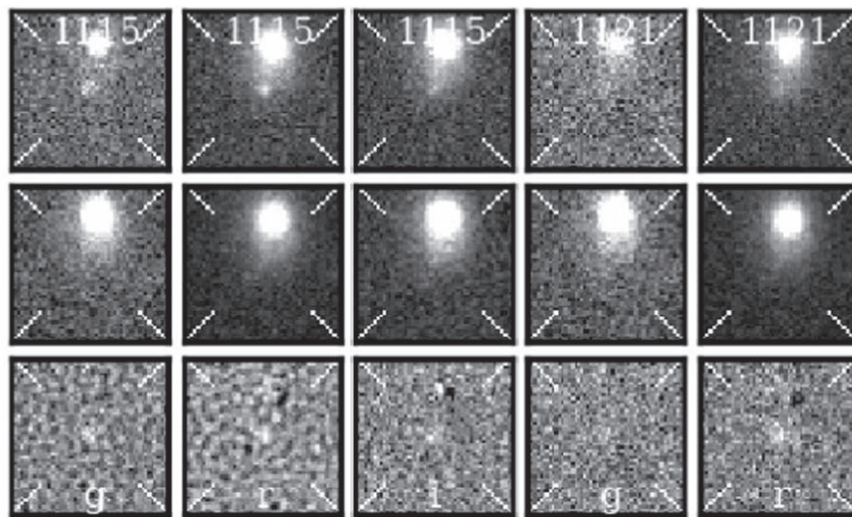


Figure 9. Image stamps for DES-Cand-2. The top row is the search image, the middle row is the template, and the bottom row is the difference image. Filters are shown at the bottom of each column, and dates are given in MMDD format at the top of each column.

derived in this analysis, so we do not claim association between either of our candidates and their corresponding neutrino alerts. Considering both follow-ups together, the observed number of SNe in the vicinity of the IceCube neutrino alert directions is compatible within 1σ to arise from fluctuations from the joint expected background.

6. Follow-up Strategy Implications

In this section, we examine whether observational follow-up campaigns can be used to determine the CC SN contribution to the teraelectronvolt to peta electronvolt IceCube neutrino flux. We base the discussion on results and analysis methods presented above and outline the requirements for a successful follow-up campaign. We then expand on the analysis by forecasting the requisite number of follow-ups to make a statistically significant statement about this problem.

6.1. Necessary Observational Components

Previous efforts have been made to associate CC SNe with neutrino telescope alerts. ROTSE and TAROT were used in optical follow-ups of 42 ANTARES neutrino alerts, reaching a

maximum r -band limiting magnitude of 18.6 with an FoV diameter of 2 deg (Adrián-Martínez et al. 2016). One neutrino doublet IceCube alert has been followed up with ROTSE and PTF, and while a CC SN was found in the FoV, it was determined to be old and type II n via spectroscopy from Keck I LRIS and Gemini/GMOS-N and therefore unassociated with the neutrinos (Aartsen et al. 2015b). The optical instruments in this effort reached a peak r -band limiting magnitude of 19.5 with an FoV diameter of 2.0 deg. Only a small fraction of cosmic neutrinos will be detected as doublets, while the large majority will be singlets. Accordingly, the follow-up of singlets is a promising approach. However, as shown by Figure 5, significantly deeper observations are required in the singlet case. Specifically, our SNANA simulations, with peak r -band magnitudes displayed in Figure 5, show the importance of DECam’s imaging depth in searches for CC SNe since the fainter SNe in the 21–23.5 mag range become detectable. A complementary version of Figure 5 where the limiting magnitude was set to 21 mag is available in Figure 10, illustrating the small fraction of all occurring SNe detectable at this optical depth. Because CC SNe are expected to follow the cosmic massive star formation rate, they are expected to be

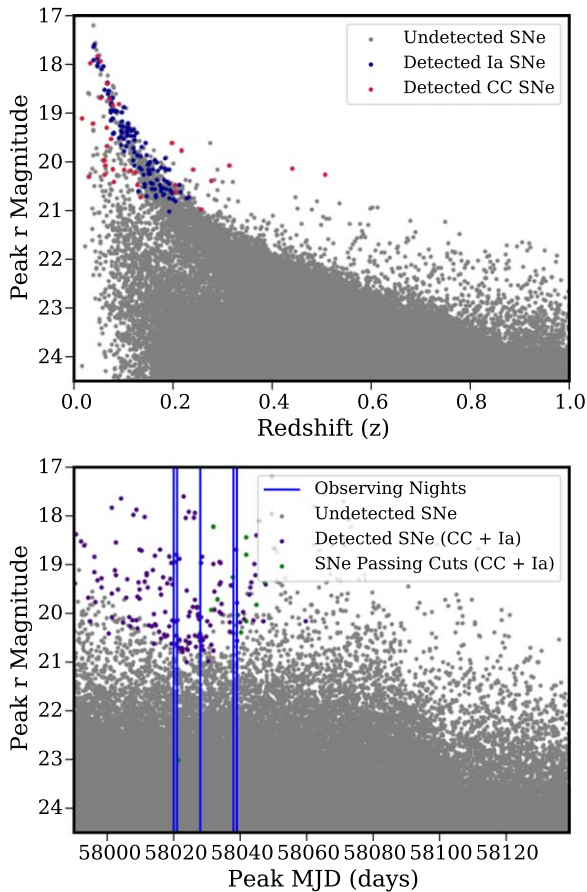


Figure 10. Background SN distribution for simulations of IC170922A with a limiting magnitude of 21 mag.

mostly distributed at higher redshifts, and hence faint in the optical bands. Therefore, it is not surprising that deep imaging offers a significant advantage to follow-up campaigns.

Even with the deep DECam observations presented in this work, detecting a CC SN as a teraelectronvolt to petaelectronvolt neutrino counterpart is still difficult, as our sensitivity analysis suggests. Our simulations and NCIP analysis show that only $\sim 9.5\%$ – 12% of associated CC SNe with $z \leq 0.3$ would be bright enough to be detectable. For $z > 0.3$, less than 1% of associated CC SNe can be detected. When we fold this low detection efficiency with the cosmic massive star formation rate as described in Section 2, unassociated SNe are expected to overwhelm the signal population. For example, based on the expected signal (0.038) and background (0.229) candidates per follow-up from Figure 7 for IC170922A, we would detect approximately four associated CC SNe and 23 unassociated SNe out to a redshift of $z = 1.0$ within the IC90 regions over the course of 100 IceCube follow-up experiments using DECam.

The redshift distribution and SN type composition of the expected background after our candidate selection pipeline are displayed in Figure 7 and are particularly useful in understanding the difficulty of claiming association between a neutrino and a CC SN. In Figure 7, the area under the dashed black curve represents the total expected number of signal events for a given follow-up.

We have multiplied the redshift probability distribution function described by the cosmic massive star formation rate by

the IceCube signalness for the alert, which was ~ 0.56 for IC170922A. This curve also follows the assumption that the entire IceCube teraelectronvolt to petaelectronvolt energy neutrino flux is caused by CC SNe, which we refer to as the $\lambda = 1.0$ case in Appendix A. We note that for low redshifts ($z \lesssim 0.2$), the redshifted neutrino energy will be very close to its rest-frame energy. Therefore, we find it sufficient to leave out the contribution of the spectral energy distribution of neutrinos from the calculation. The red curve then folds the black curve with the signal detection efficiency from Figure 6 to obtain the expected number of detected CC SN teraelectronvolt to petaelectronvolt neutrino counterparts per follow-up as a function of redshift. In the redshift range where the red curve is nonvanishing, we note that the most dominant background is CC SNe that are present in the FoV but are not associated with the neutrino. These CC SNe have also passed the rising and phase cuts of our pipeline, meaning they appear to be temporally coincident with a neutrino as well. Therefore, the largest background in this analysis is CC SNe that are temporally coincident with the neutrino, which unfortunately are the exact characteristics of our signal population.

Given this background, our main tool for determining if a given candidate is associated with the neutrino alert is the proximity of the candidate to the alert centroid. Additional differentiating features between signal and background samples are the candidate redshift and spectroscopic characterization. The redshift can likely be determined to sufficient accuracy based on a photometric redshift of the host galaxy, but if spectra can be obtained, then it would also be possible to exclude the type Ia SNe background.

6.2. Forecasting Statistical Significance

An individual follow-up with deep optical imaging, triggered observations, and redshift information for all candidates is still unlikely to reach a meaningful level of significance due to a signal-like background of unassociated CC SNe that are coincident in time with neutrino alerts and a low signal detection efficiency. Therefore, we frame this analysis as seeking to detect an excess of CC SNe located near IceCube neutrino alerts in space and time over the course of multiple follow-ups. We present a full calculation later in this section, but we outline the basis of it here and restrict our focus to the IC90 region for clarity; the full calculation utilizes the entire DECam FoV. In the IC90 region, from Figure 7 we expect 0.038 signal events and 0.229 background events for a follow-up similar to IC170922A, and from Figure 14 we expect 0.047 signal events and 0.067 background events for a follow-up similar to IC171106A. In the full calculation, if redshift information is available, the contribution to the total significance is weighted by the expected number of signal and background events at the particular redshift. Overall, this process just reduces the contribution of background events to the total significance, so we can account for the effect of having redshift information for a candidate by dividing the expected background by a factor of ~ 3 to simulate a smaller redshift range. Applying this factor and averaging the results lead to a mean expected 0.043 signal events and a mean expected 0.049 background events. We then estimate the significance after N follow-ups using a Poisson distribution:

$$p\text{-value} = 1 - \text{PoissonCDF}(\text{Observed}|\text{Expected}). \quad (4)$$

Setting the “Expected” number of events to be $N \times 0.049$ for the background-only null hypothesis and setting the

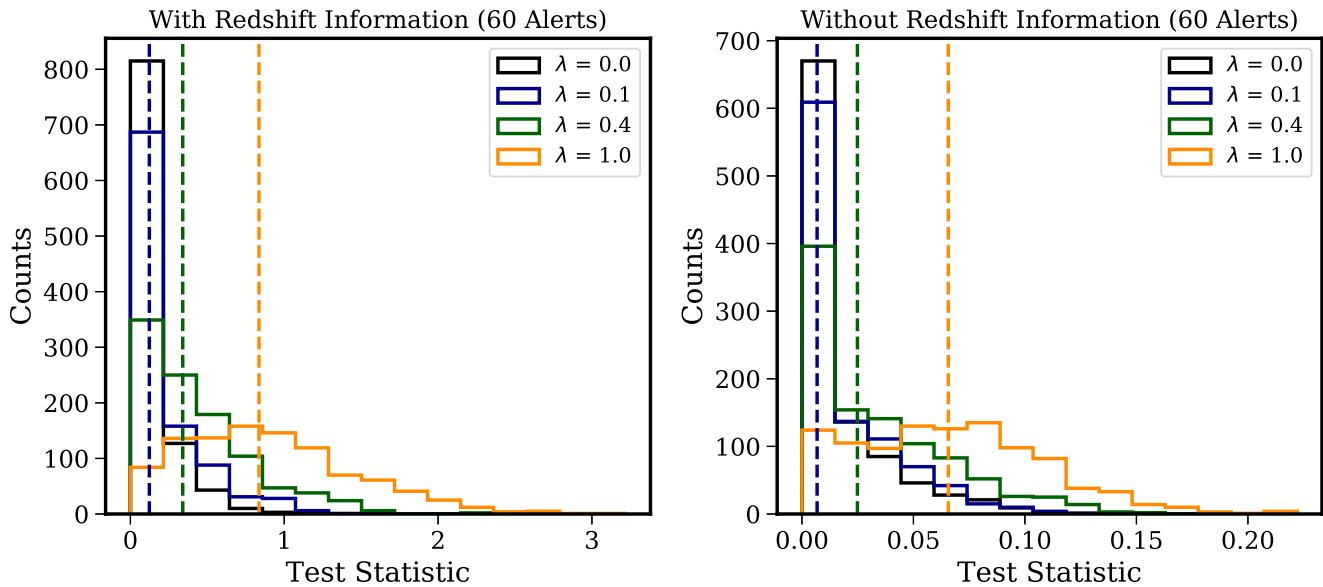


Figure 11. Test statistic distributions for 1000 realizations of the follow-up of 60 IceCube alerts with DECam parameterized by the expected fraction of IceCube events caused by CC SNe (λ). The left/right panel displays the test statistic distribution with/without redshift information available for all alerts. The median values of the signal-hypothesis test statistic distributions are also displayed.

“Observed” number of events to be $N \times (0.043 + 0.049)$ enable us to evaluate the significance as a function of the number of follow-ups. As well, one can see that increasing the number of follow-ups will increase the global significance. In this brief calculation, for 100 follow-ups, we would expect to reach a p value of ~ 0.029 , which is between 2σ and 3σ . The addition of positional information and a more accurate accounting of redshift information in the full calculation both increase the significance beyond this simplified example.

To make this calculation more rigorous, we simulate pipeline candidate events with frequencies matching the mean expected event rates from the two follow-ups. To determine the probability of an NCIP candidate being the source of the neutrino, we evaluate the candidate’s position and redshift in the context of the expected signal and background population distributions of these quantities. For the signal sample, we fit independent 2D asymmetric Gaussian distributions to the 90% confidence level error bounds on the R.A. and decl. We multiply our detection efficiency by the fraction of events that would fall on a DECam CCD to account for chip gaps and the few events that fall outside the DECam FoV. For the background distribution, we adopt a uniform distribution of events on the individual DECam CCDs. The redshift distributions for the signal and background samples are taken from Figure 7. Using these distributions, we assess whether CC SNe contribute to the teraelectronvolt to petaelectronvolt neutrino flux by searching for an excess of temporally coincident CC SNe in our observations compared to the expected background contamination rate. Appendix A explains this process in greater detail and provides an overview of the maximum-likelihood formalism used to quantify the likelihood of association between our pipeline candidates and IceCube neutrino alerts.

Using the maximum-likelihood framework and the angular and redshift distributions for the signal and background samples, we perform 1000 realizations of optical follow-up campaigns of IceCube alerts. For each alert follow-up, we determine a list of candidates by sampling the signal and

background event distributions. The list of candidates has a probability of containing a signal event of $0.038 \times 0.89 = 0.0338$ for the IC170922A follow-up, where 0.038 is the expected number of detected signal events per follow-up from Figure 7 and 0.89 is the fraction of the signal that falls on the DECam CCDs. The number of expected background events per follow-up (0.717) is determined from the background AUC in Figure 7 by scaling the value to the full DECam FoV. The number of background events to simulate is then determined by a Poisson probability distribution with a mean of 0.717. Once the number of candidates has been determined, we sample the angular and redshift distributions to obtain a realistic representation of the follow-up. We also introduce a signal normalization parameter, λ , which represents the fraction of the teraelectronvolt to petaelectronvolt neutrino flux caused by CC SNe, and we perform the realizations under different values of λ .

The test statistic distributions for 1000 realizations of follow-up campaigns of 60 alerts based on the conditions of both alerts are displayed in Figure 11. We determine the significance level at which we would be able to claim CC SNe contribute to the teraelectronvolt to petaelectronvolt IceCube flux by taking the median value of our alternative-hypothesis ($\lambda \neq 0.0$) distributions and calculating the fraction of the null-hypothesis distribution ($\lambda = 0.0$) greater than the median test statistic. This fraction can be interpreted as the frequentist p value. Figure 11 shows that our sensitivity for detecting an excess of CC SNe temporally and spatially coincident with IceCube alerts is greater when redshift information is available and if CC SNe make up a large fraction of the teraelectronvolt to petaelectronvolt neutrino flux.

We then further the analysis of the viability of this type of study by calculating the discovery potential for follow-up campaigns with increasing numbers of alerts. The result of this calculation is displayed for the same three values of λ in Figure 8. The cases of every candidate having available redshift information and no candidates having available redshift information are taken as the boundary cases of the best- and

worst-case scenarios. We note that a few alerts are required before the p value is expected to differ from 1.0 in all cases, but that this behavior is explained by the fact that we use the median test statistic to calculate the p value. The p value is the fraction of null-hypothesis test statistics strictly greater than the median of the signal-hypothesis test statistic distributions, so the median must be larger than zero in order to produce a p value less than one. Due to the low detection efficiency of signal events, follow-up campaigns of few alerts are very likely to be statistically consistent with the background and hence produce test statistic distributions that are predominantly composed of test statistics of zero. Based on this calculation, optical follow-up campaigns of this nature would require approximately 60 follow-ups before an excess of temporally and spatially coincident CC SNe could be detected at the 3σ confidence level in the case that photometric redshift information is available for each candidate and that CC SNe account for 100% of the teraelectronvolt to petaelectronvolt neutrino flux. In the less optimistic case where CC SNe account for a smaller percentage of the teraelectronvolt to petaelectronvolt neutrinos, or redshift information is unable to be obtained, the required number of follow-ups can easily exceed 200. The IceCube event rate is approximately one alert per month, and typically one in every three alerts is observable from CTIO based on solar and atmospheric conditions.

This analysis highlights several vital components for successful optical follow-ups of IceCube neutrino alerts searching for CC SNe. First, deep imaging is needed to efficiently detect CC SNe counterparts to teraelectronvolt to petaelectronvolt neutrinos at $z \sim 0.1$, as shown by the comparison between Figures 5 and 10. A sufficiently large FoV is also required such that the IceCube localization region can be covered. DECam's ~ 23.5 r -band limiting magnitude in 90 second exposures and ~ 3 deg² FoV make it the current imager of choice in the southern hemisphere for this task. Even with DECam, we anticipate a large background of CC SNe that are unassociated with the teraelectronvolt to petaelectronvolt neutrinos and difficult to distinguish from neutrino-causing CC SNe. Photometric redshifts and spectroscopic characterization can help with the differentiation, but with the low IceCube event rate and optical detection efficiency of CC SNe, a follow-up campaign would take several years to be able to observe a significant excess of CC SNe near IceCube alerts. It is also possible that tightened constraints on the CC SNe luminosity function and SNe rise times will improve the accuracy of the simulations used in this analysis and in the significance forecasting. It is anticipated that an expansion of the IceCube detector or improved real-time alert selection could increase the event rate and improve the angular resolution of neutrino reconstruction.

7. Conclusion

The real-time alert system for IceCube neutrinos has made possible the detection of electromagnetic counterparts for transient high-energy astrophysical events. Using this system, we test whether CC SNe contribute to the largely unexplained teraelectronvolt to petaelectronvolt IceCube neutrino flux via a prompt relativistic jet mechanism during the collapse. In this study, we followed up two IceCube alerts from 2017 September 22 (IC170922A) and 2017 November 6 (IC170922A) with photometric observations in optical wavelengths using DECam. These pilot observations combine the deepest-to-date optical follow-up observations of teraelectronvolt to petaelectronvolt

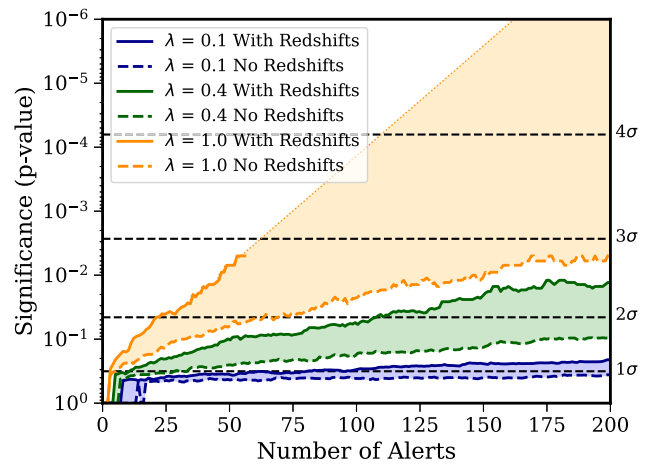


Figure 12. Projected significance levels for DECam follow-up campaigns with increasing numbers of alerts based on the expected numbers of signal and background events in the IC170922A and IC171106A follow-ups. We display the relationship under different values of the parameter λ , which represents the true fraction of the IceCube teraelectronvolt to petaelectronvolt neutrino flux caused by CC SNe. We performed 1000 realizations of each follow-up campaign and calculate the p value by comparing the median test statistic to the null-hypothesis test statistic distribution. Since we only performed 1000 realizations, we are unable to probe p values lower than 0.001, so we extrapolate all p values smaller than 0.001.

IceCube neutrinos with a detailed estimation of the relevant backgrounds and a maximum-likelihood analysis to fully characterize our sensitivity to CC SNe.

We developed and validated an automated candidate selection pipeline (NCIP) based on SNe simulations matched to our observing cadence and conditions. Between the two alerts, NCIP found two plausible neutrino source candidate SNe (DES-Cand-1 for IC170922A and DES-Cand-2 for IC171106A) based on light curve properties and temporal coincidence. Both candidate SNe are located outside the respective 90% confidence localization regions from IceCube. Applying a maximum-likelihood analysis to our candidates based on the simulated SNe background and spatial coincidence, we find that the two observed candidates are consistent with background unassociated SNe (p value = 0.093). Other multimessenger observations suggest that IC170922A is associated with the flaring gamma-ray blazar TXS 0506+056.

To assess the viability of continued optical searches triggered by IceCube alerts, we perform 1000 realizations of follow-up campaigns of up to 200 alerts. We find that approximately 60 follow-ups are required to reach the 3σ confidence level in the case that the astrophysical neutrino flux is contributed entirely by CC SNe and redshifts are available for all detected candidates (Figure 12). Without the availability of photometric redshift information for all candidates, the requisite number of follow-ups rises to ~ 200 to make the same statement. Furthermore, if neutrinos from relativistic jets inside CC SNe do not make up a large percentage of the teraelectronvolt to petaelectronvolt neutrino flux, the number of follow-ups required to achieve a high confidence detection could be much larger. The sensitivity is limited primarily by the rate of unassociated low-redshift CC SNe that explode in spatial and temporal coincidence with the neutrino alerts. This residual background is degenerate with the signal population and therefore challenging to further reduce. Based on the methods presented here and the current rate of HESE and EHE real-time

alerts from IceCube, a sustained optical follow-up program using a few hours of DECam time per semester extending over $\gtrsim 10$ yr would be needed to determine whether CC SNe contribute to the neutrino flux.

R. Morgan thanks the LSSTC Data Science Fellowship Program, which is funded by LSSTC, NSF Cybertraining grant No. 1829740, the Brinson Foundation, and the Moore Foundation; his participation in the program has benefited this work.

All authors thank Sahar Allam, Agnes Ferté Indiarose Friswell, Kate Furnell, Mandeep Gill, Michael Johnson, Nikolay Kuropatkina, Marty Murphy, Douglas Tucker, Noah Weaverdyck, Reese Wilkinson, Hao-Yi Wu, and Brian Yanny for operating Blanco/DECam and for their help in performing the follow-ups presented in this work. We also thank Douglas Finkbeiner, Abi Saha, Malhorta Sangeeta, Eddie Schlafly, Monika Soraisam, Scott Sheppard, and Catherine Zucker for operating Blanco/DECam during more recent follow-ups.

This work was completed in part with resources provided by the University of Chicago Research Computing Center.

Funding for the DES projects has been provided by the U.S. Department of Energy, the U.S. National Science Foundation, the Ministry of Science and Education of Spain, the Science and Technology Facilities Council of the United Kingdom, the Higher Education Funding Council for England, the National Center for Supercomputing Applications at the University of Illinois at Urbana-Champaign, the Kavli Institute of Cosmological Physics at the University of Chicago, the Center for Cosmology and Astro-Particle Physics at The Ohio State University, the Mitchell Institute for Fundamental Physics and Astronomy at Texas A&M University, Financiadora de Estudos e Projetos, Fundação Carlos Chagas Filho de Amparo à Pesquisa do Estado do Rio de Janeiro, Conselho Nacional de Desenvolvimento Científico e Tecnológico and the Ministério da Ciência, Tecnologia e Inovação, the Deutsche Forschungsgemeinschaft, and the Collaborating Institutions in the Dark Energy Survey.

The Collaborating Institutions are Argonne National Laboratory, the University of California at Santa Cruz, the University of Cambridge, Centro de Investigaciones Energéticas, Medioambientales y Tecnológicas-Madrid, the University of Chicago, University College London, the DES-Brazil Consortium, the University of Edinburgh, the Eidgenössische Technische Hochschule (ETH) Zürich, Fermi National Accelerator Laboratory, the University of Illinois at Urbana-Champaign, the Institut de Ciències de l’Espai (IEEC/CSIC), the Institut de Física d’Altes Energies, Lawrence Berkeley National Laboratory, the Ludwig-Maximilians Universität München and the associated Excellence Cluster Universe, the University of Michigan, the National Optical Astronomy Observatory, the University of Nottingham, The Ohio State University, the University of Pennsylvania, the University of Portsmouth, SLAC National Accelerator Laboratory, Stanford University, the University of Sussex, Texas A&M University, and the OzDES Membership Consortium.

This work is based in part on observations at Cerro Tololo Inter-American Observatory, National Optical Astronomy Observatory, which is operated by the Association of Universities for Research in Astronomy (AURA) under a cooperative agreement with the National Science Foundation.

The DES data management system is supported by the National Science Foundation under grant Nos. AST-1138766 and AST-1536171. The DES participants from Spanish institutions are partially supported by MINECO under grants AYA2015-

71825, ESP2015-88861, FPA2015-68048, SEV-2012-0234, SEV-2016-0597, and MDM-2015-0509, some of which include ERDF funds from the European Union. IFAE is partially funded by the CERCA program of the Generalitat de Catalunya. Research leading to these results has received funding from the European Research Council under the European Union’s Seventh Framework Program (FP7/2007–2013) including ERC grant agreements 240672, 291329, and 306478. We acknowledge support from the Australian Research Council Centre of Excellence for All-sky Astrophysics (CAASTRO), through project No. CE110001020.

This manuscript has been authored by Fermi Research Alliance, LLC, under contract No. DE-AC02-07CH11359 with the U.S. Department of Energy, Office of Science, Office of High Energy Physics. The United States Government retains and the publisher, by accepting the article for publication, acknowledges that the United States Government retains a nonexclusive, paid-up, irrevocable, world-wide license to publish or reproduce the published form of this manuscript, or allow others to do so, for United States Government purposes.

Facility: Blanco (DECam).

Software: PSNID (Sako et al. 2011), SNANA (Kessler et al. 2009), matplotlib (Hunter 2007), pandas (McKinney 2010), numpy (Van Der Walt et al. 2011), sci-kit learn (Pedregosa et al. 2011), scipy (Jones et al. 2001).

Appendix A Maximum-likelihood Formalism

In this appendix, we describe the formalism used to quantify the statistical power of our analysis in terms of testing the hypothesis that CC SNe contribute to the IceCube high-energy neutrino flux. We perform a maximum-likelihood analysis in redshift-position space to determine the significance of observed excesses of CC SNe at the location and times of IceCube neutrino alerts.

From our SNANA simulations of the two events, we have determined the redshift distribution of our expected signal and background populations. These distributions are displayed in Figure 7 for IC170922A and in Figure 14 for IC171106A. The black curves in these figures will be referred to as $\xi S_z(z)$, where ξ is the IceCube signalness and $S_z(z)$ is the probability density function for signal events in redshift space given by Equation (1). The number of detected signal events per unit redshift (red curve in these figures) is derived from the black curve through a multiplication by the optical detection efficiency as a function of redshift $\varepsilon(z)$, so we express this quantity as $\xi S_z(z) \varepsilon(z)$. It is necessary at this point to introduce a signal normalization parameter λ , which will represent the total fraction of the IceCube teraelectronvolt to petaelectronvolt flux caused by CC SNe. Therefore, over several follow-ups, the expectation value of λ will be the fraction of IceCube neutrinos caused by CC SNe. Thus, the expected number of signal events per unit redshift is $\lambda \xi S_z(z) \varepsilon(z)$. The expected number of background events per unit redshift is represented by the curves labeled “Remaining Background” in Figures 7 and 14, and we express this function in our formalism as $B_z(z)$.

We distribute the events in position space according to a uniform distribution across the DECam FoV for the background population and according to a 2D asymmetric Gaussian fit to the 90% confidence interval containment region determined by IceCube for the signal population. The signal and background distributions for angular space are expressed as

$S_\Omega(\Omega)$ and $B_\Omega(\Omega)$, which are normalized probability distribution functions. Therefore, $\lambda \xi S_z(z) \varepsilon(z) S_\Omega(\Omega)$ is the expected number of signal events per unit redshift per unit solid angle selected by our pipeline for a given follow-up, and $B_z(z) B_\Omega(\Omega)$ is the expected number of background events per unit redshift per unit solid angle selected by our pipeline for a given follow-up.

Suppose that after a single follow-up, we find one candidate (which we will denote as Candidate i) that passes all selection criteria. Consider two cases: redshift information being available for Candidate i and redshift information not being available for Candidate i . In these two separate cases, we can write the model-expected numbers of events as

$$m_i(\lambda) = \int dz d\Omega \delta(z - z_i) \delta(\Omega - \Omega_i) [\lambda \xi S_z(z) \varepsilon(z) S_\Omega(\Omega) + B_z(z) B_\Omega(\Omega)] \text{ with redshift information and}$$

$$m_i(\lambda) = \int dz d\Omega \delta(\Omega - \Omega_i) [\lambda \xi S_z(z) \varepsilon(z) S_\Omega(\Omega) + B_z(z) B_\Omega(\Omega)] \text{ without redshift information,}$$

where we integrate from redshift $z = 0$ to $z = 1$ and over the entire DECam FoV. The delta functions serve to evaluate the expected numbers of signal and background event functions at the position and redshift of Candidate i . Therefore, in the case without available redshift information, we get contributions from all redshifts between $z = 0$ and $z = 1$. To make the discussion more straightforward, we will adopt the following shorthand notation:

$$S_i \equiv \int dz d\Omega \delta(z - z_i) \delta(\Omega - \Omega_i) \xi S_z(z) \varepsilon(z) S_\Omega(\Omega) \quad \text{and}$$

$$B_i \equiv \int dz d\Omega \delta(z - z_i) \delta(\Omega - \Omega_i) B_z(z) B_\Omega(\Omega),$$

where it is to be understood that in the case without available redshift information for Candidate i , S_i and B_i are defined without the $\delta(z - z_i)$ term, implying the need to include the contributions from all redshifts. Therefore, we can write $m_i(\lambda) = \lambda S_i + B_i$.

Now assuming the model of expected counts follows a Poisson distribution, we can write the likelihood and log-likelihood of observing k candidates in a given follow-up as the product of probabilities of observing k_j objects in redshift-spatial bin j as

$$\mathcal{L} = \prod_{j=1}^{N \text{ bins}} \frac{[m_j(\lambda)]^{k_j} e^{-m_j(\lambda)}}{k_j!}$$

$$\Rightarrow \log(\mathcal{L}) = \sum_{j=1}^{N \text{ bins}} \log \left(\frac{[m_j(\lambda)]^{k_j} e^{-m_j(\lambda)}}{k_j!} \right)$$

$$\Rightarrow \log(\mathcal{L}) = \sum_{j=1}^{N \text{ bins}} (k_j \log(m_j(\lambda)) - m_j(\lambda) - \log(k_j!)).$$

In the limit of vanishingly small redshift-spatial bins where each bin contains either one or zero objects, we can express the log-likelihood as

$$\log(\mathcal{L}) = \left[\sum_{i=1}^{N \text{ candidates}} \log(m_i(\lambda)) \right] - \int dz d\Omega m(\lambda),$$

where the first term comes from evaluating the $k_j \log(m_j(\lambda))$ and $\log(k_j!)$ terms for $k_j = 0$ and $k_j = 1$, and the second term is

the evaluation of the sum of expected model counts over all bins, regardless of the presence of candidates. Dropping all terms that are independent of λ , since they do not contribute in the maximization, we can write

$$\log(\mathcal{L}) = \left[\sum_{i=1}^{N \text{ candidates}} \log(\lambda S_i + B_i) \right] - f\lambda,$$

where $f \equiv \int dz d\Omega \xi S_z(z) \varepsilon(z) S_\Omega(z)$.

The value of f can be recognized as the area under the ‘‘Detected Signal’’ curve in Figures 7 and 14 multiplied by the fraction of signal events that would fall on a CCD in our 2D asymmetric Gaussian distribution of signal events.

Maximizing the log-likelihood with respect to λ via $\partial \log(\mathcal{L}) / \partial \lambda = 0$ and multiplying by $\hat{\lambda}$, we obtain a maximization condition in terms of the individual probabilities for each candidate to be associated with the neutrino alert:

$$f \hat{\lambda} = \sum_{i=1}^{N \text{ candidates}} \frac{\hat{\lambda} S_i}{\hat{\lambda} S_i + B_i} \equiv \sum_{i=1}^{N \text{ candidates}} p_i,$$

where $\hat{\lambda}$ is the optimum value of λ that satisfies this above condition. Operating under this condition that maximizes the log-likelihood, we can use the delta log-likelihood to characterize the significance of a follow-up detecting a certain amount of excess temporally and spatially coincident CC SNe:

$$\Delta \log(\mathcal{L}) = \log(\mathcal{L})|_{\lambda=\hat{\lambda}} - \log(\mathcal{L})|_{\lambda=0}.$$

Over a sequence of follow-up observations, then, we define our test statistic (TS) to be the sum of the delta log-likelihoods of all the constituent follow-ups:

$$\text{TS} = \sum_{n=1}^{N \text{ follow-ups}} (\Delta \log(\mathcal{L}))_n.$$

For a follow-up campaign that observes a given number of SN candidates, we can evaluate the significance of the claim that the number of candidates observed is greater than the expected background and hence likely linked to the IceCube neutrino alerts by comparing the calculated TS value to the null-hypothesis TS distribution. In this work, we obtain the null-hypothesis TS distribution by performing 1000 realizations of follow-up campaigns with λ set to 0.0. To obtain our signal-hypothesis TS value for a given value of λ , we perform the 1000 realizations and take the median of the distribution to be our signal TS value. The p value for this test is the fraction of the null-hypothesis distribution that is larger than the median signal-hypothesis TS value, allowing for a direct evaluation of the significance level at which we can claim CC SNe contribute to the teraelectronvolt to petaelectronvolt IceCube neutrino flux.

Appendix B Additional Figures

In this appendix, we provide complementary figures to those presented in the analysis. Figure 13 shows the the signal and background detection efficiencies for the IC171106A follow-up. Figure 14 shows the expected number of signal and background events to pass our selection criteria in the IC171106A follow-up. Figure 15 shows the signal and background detection efficiency for a follow-up with similar observing conditions to IC170922A where the 5σ limiting

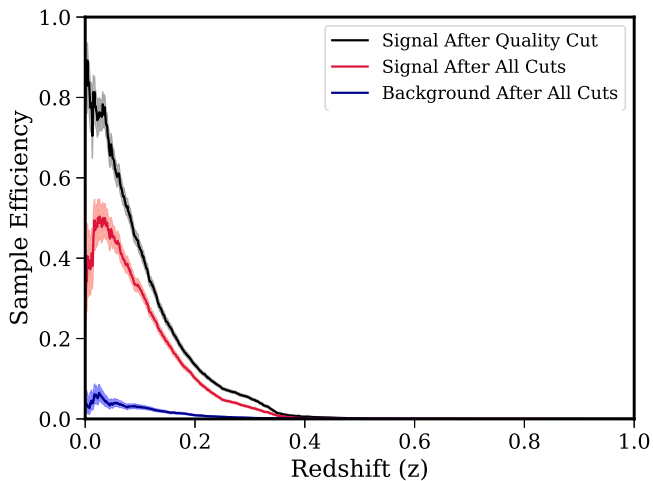


Figure 13. Detection efficiency parameterized by redshift for the signal and background populations for the IC171106A alert follow-up.

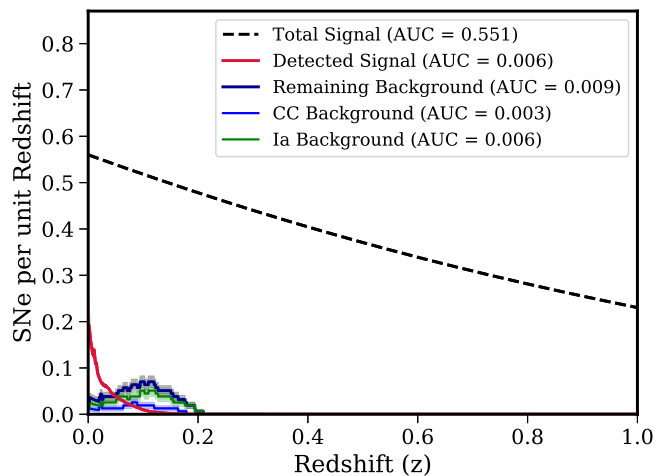


Figure 16. Expected events at a given redshift based on simulations of the IC170922A follow-up with limiting magnitude 21. Shaded error regions give a 68% confidence interval for the signal curve and a standard Poisson statistical uncertainty for the background curves.

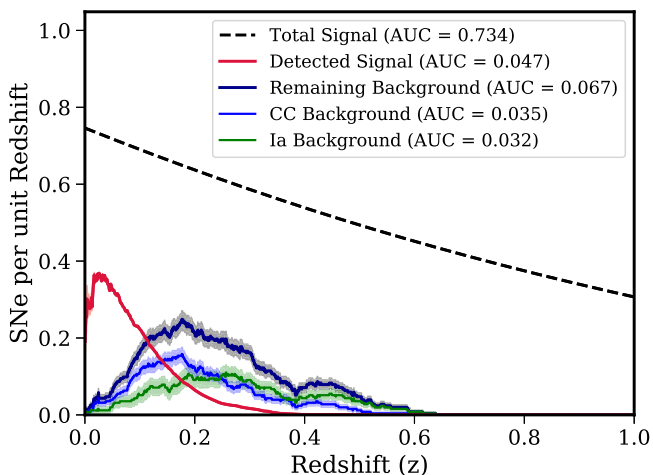


Figure 14. Expected events at a given redshift based on simulations of the IC171106A follow-up.

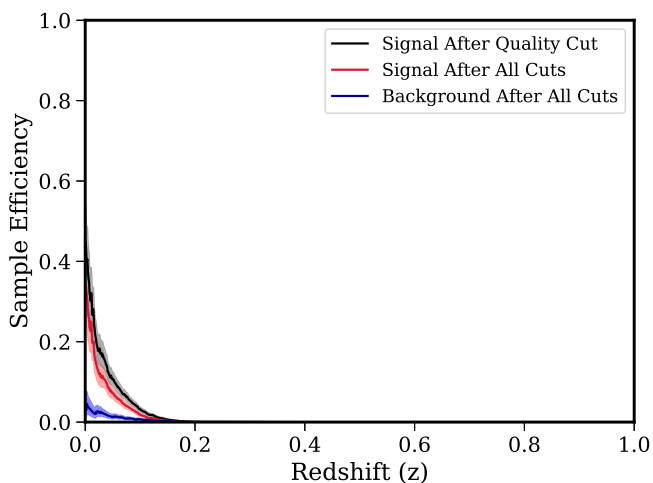
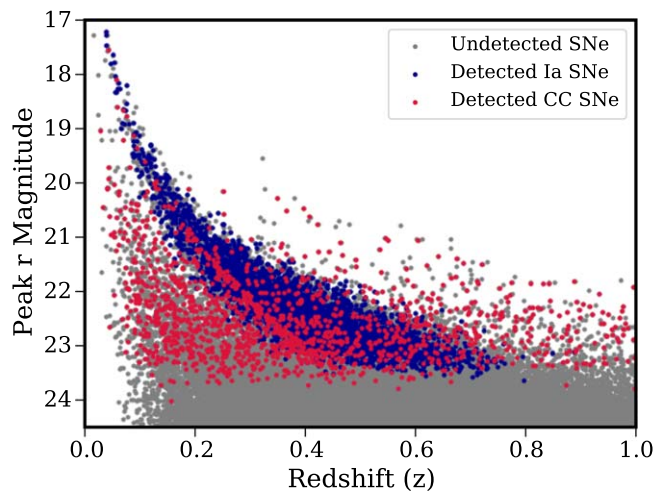


Figure 15. Detection efficiency as a function of redshift for simulations of IC170922A with a limiting magnitude of 21 mag.

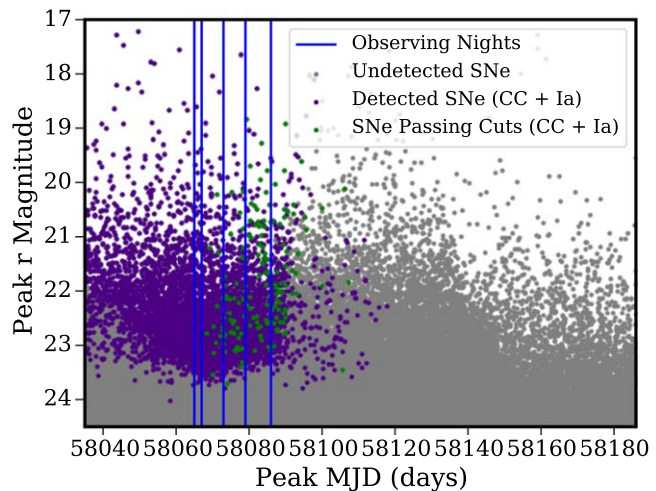












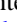







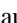










Figure 17. Background SN distribution for simulations of IC171106A with a limiting magnitude of 23.5 mag.

magnitude is 21 mag. Figure 16 shows the expected signal and background events per unit redshift to pass our selection criteria for a follow-up with similar observing conditions to IC170922A where the 5σ limiting magnitude is 21 mag. Figure 17 shows peak r -band magnitude distribution as functions of the date of the peak flux and the redshift of the SNe for simulated SNe under the conditions of the IC171106A follow-up.

ORCID iDs

R. Morgan  <https://orcid.org/0000-0002-7016-5471>
 R. Kessler  <https://orcid.org/0000-0003-3221-0419>
 A. Franckowiak  <https://orcid.org/0000-0002-5605-2219>
 A. Palmese  <https://orcid.org/0000-0002-6011-0530>
 A. K. Vivas  <https://orcid.org/0000-0003-4341-6172>
 A. Drlica-Wagner  <https://orcid.org/0000-0001-8251-933X>
 E. Neilsen  <https://orcid.org/0000-0002-7357-031>
 H. T. Diehl  <https://orcid.org/0000-0002-8357-7467>
 M. Soares-Santos  <https://orcid.org/0000-0001-6082-8529>
 M. Carrasco Kind  <https://orcid.org/0000-0002-4802-3194>
 J. Carretero  <https://orcid.org/0000-0002-3130-0204>
 J. De Vicente  <https://orcid.org/0000-0001-8318-6813>
 S. Desai  <https://orcid.org/0000-0002-0466-3288>
 J. Frieman  <https://orcid.org/0000-0003-4079-3263>
 J. García-Bellido  <https://orcid.org/0000-0002-9370-8360>
 D. W. Gerdes  <https://orcid.org/0000-0001-6942-2736>
 G. Gutierrez  <https://orcid.org/0000-0003-0825-0517>
 N. Kuropatkin  <https://orcid.org/0000-0003-2511-0946>
 J. L. Marshall  <https://orcid.org/0000-0003-0710-9474>
 F. Menanteau  <https://orcid.org/0000-0002-1372-2534>
 R. Miquel  <https://orcid.org/0000-0002-6610-4836>
 A. A. Plazas  <https://orcid.org/0000-0002-2598-0514>
 E. Sanchez  <https://orcid.org/0000-0002-9646-8198>
 M. Smith  <https://orcid.org/0000-0002-3321-1432>
 F. Sobreira  <https://orcid.org/0000-0002-7822-0658>
 E. Suchyta  <https://orcid.org/0000-0002-7047-9358>
 G. Tarle  <https://orcid.org/0000-0003-1704-0781>
 A. R. Walker  <https://orcid.org/0000-0002-7123-8943>
 J. Weller  <https://orcid.org/0000-0002-8282-2010>

References

- Aartsen, M., Ackermann, M., Adams, J., et al. 2017a, *APh*, **92**, 30
 Aartsen, M., Ackermann, M., Adams, J., et al. 2017b, *JInst*, **12**, P03012
 Aartsen, M. G., Abbasi, R., Ackermann, M., et al. 2014, *JInst*, **9**, P03009
 Aartsen, M. G., Abraham, K., Ackermann, M., et al. 2015a, *ApJ*, **809**, 98
 Aartsen, M. G., Abraham, K., Ackermann, M., et al. 2015b, *ApJ*, **811**, 52
 Aartsen, M. G., Abraham, K., Ackermann, M., et al. 2017c, *ApJ*, **835**, 45
 Aartsen, M. G., Abraham, K., Ackermann, M., et al. 2017d, *ApJ*, **835**, 151
 Aartsen, M. G., Ackermann, M., Adams, J., et al. 2015c, *ApJL*, **805**, L5
 Abbasi, R., Abdou, Y., Abu-Zayyad, T., et al. 2011, *PhRvD*, **84**, 082001
 Abbasi, R., Abdou, Y., Abu-Zayyad, T., et al. 2012, *A&A*, **539**, A60
 Abbott, T. M. C., Abdalla, F. B., Alarcon, A., et al. 2018, *PhRvD*, **98**, 043526
 Adrián-Martínez, S., Ageron, M., Albert, A., et al. 2016, *JCAP*, **2016**, 062
 Ahlers, M., Bai, Y., Barger, V., & Lu, R. 2016, *PhRvD*, **93**, 013009
 Ando, S., & Beacom, J. F. 2005, *PhRvL*, **95**, 061103
 Bailey, S., Aragon, C., Romano, R., et al. 2007, *ApJ*, **665**, 1246
 Baret, B., & Elewcky, V. V. 2011, *RPPH*, **74**, 046902
 Barthelmy, S. D., Butterworth, P., Cline, T. L., et al. 1998, in AIP Conf. Proc. 428, 4th Huntsville Gamma-Ray Burst Symp., ed. C. A. Meegan et al. (Melville, NY: AIP), 99
 Beall, J. H. 2006, *ChJAA*, **6**, 174
 Bechtol, K., Ahlers, M., Mauro, M. D., Ajello, M., & Vandenbroucke, J. 2017, *ApJ*, **836**, 47
 Bernstein, J. P., Kessler, R., Kuhlmann, S., et al. 2012, *ApJ*, **753**, 152
 Breiman, L. 2001, *Mach. Learn.*, **45**, 5
 Burrows, A., Hayes, J., & Fryxell, B. A. 1995, *ApJ*, **450**, 830
 Caprioli, D. 2015, *ApJL*, **811**, L38
 Chiarusi, T., & Spurio, M. 2010, *EPJC*, **65**, 649
 Dermer, C. D., & Atoyan, A. 2003, *PhRvL*, **91**, 071102
 Dilday, B., Kessler, R., Frieman, J. A., et al. 2008, *ApJ*, **682**, 262
 Flaugher, B., Diehl, H. T., Honscheid, K., et al. 2015, *AJ*, **150**, 150
 Franckowiak, A. 2017, *J. Phys. Conf. Ser.*, **888**, 012009
 Gaisser, T. K., & Stanev, T. 1987, *PhRvL*, **58**, 1695
 Goldstein, D. A., D'Andrea, C. B., Fischer, J. A., et al. 2015, *AJ*, **150**, 82
 González-Gaitán, S., Tominaga, N., Molina, J., et al. 2015, *MNRAS*, **451**, 2212
 Guy, Sullivan, M., Conley, A., et al. 2010, *A&A*, **523**, A7
 Hunter, J. D. 2007, *CSE*, **9**, 90
 IceCube Collaboration 2013, *Sci*, **342**, 1242856
 IceCube Collaboration 2018a, IceCube catalog of alert events up through IceCube-170922A, doi:10.21234/B4KS6S
 IceCube Collaboration 2018b, *Sci*, **36**, 147
 IceCube Collaboration, Aartsen, M. G., Ackermann, M., et al. 2017, *A&A*, **607**, A115
 IceCube Collaboration, Aartsen, M. G., Ackermann, M., et al. 2018, *Sci*, **361**, 1378
 Jones, E., Oliphant, T., Peterson, P., et al. 2001, SciPy: Open Source Scientific Tools for Python, <http://www.scipy.org/>
 Kankare, E., Huber, M., Smartt, S. J., et al. 2019, *A&A*, **626**, A117
 Keivani, A., Ayala, H., & DeLaunay, J. 2017, *Proc. ICRC (Busan)*, **35**, 629
 Kessler, R., Bassett, B., Belov, P., et al. 2010, *PASP*, **122**, 1415
 Kessler, R., Bernstein, J. P., Cinabro, D., et al. 2009, *PASP*, **121**, 1028
 Kessler, R., Marriner, J., Childress, M., et al. 2015, *AJ*, **150**, 172
 Kowalski, M., & Mohr, A. 2007, *Aph*, **27**, 533
 Li, W., Leaman, J., Chornock, R., et al. 2011, *MNRAS*, **412**, 1441
 Macaulay, E., Nichol, R. C., Bacon, D., et al. 2019, *MNRAS*, **486**, 2184
 Madau, P., & Dickinson, M. 2014, *ARA&A*, **52**, 415
 McKinney, W. 2010, in Proc. 9th Python in Science Conf., ed. S. van der Walt & J. Millman (Austin, TX: SciPy), 51
 Mészáros, P., & Waxman, E. 2001, *PhRvL*, **87**, 171102
 Mohr, J. J., Armstrong, R., Bertin, E., et al. 2012, *Proc. SPIE*, **8451**, 84510
 Murase, K., & Ioka, K. 2013, *PhRvL*, **111**, 121102
 Pedregosa, F., Varoquaux, G., Gramfort, A., et al. 2011, *J. Mach. Learn. Res.*, **12**, 2825
 Razzaque, S., Mészáros, P., & Waxman, E. 2004, *PhRvL*, **93**, 181101
 Sadeh, I., Abdalla, F. B., & Lahav, O. 2016, *PASP*, **128**, 104502
 Sako, M., Bassett, B., Connolly, B., et al. 2011, *ApJ*, **738**, 162
 Senno, N., Murase, K., & Mészáros, P. 2016, *PhRvD*, **93**, 083003
 Silberberg, R., & Shapiro, M. M. 1979, Proc. ICRC, **10**, 357
 Smith, M., Fox, D., Cowen, D., et al. 2013, *Aph*, **45**, 56
 Soares-Santos, M., Palmese, A., Hartley, W., et al. 2019, *ApJL*, **876**, L7
 Strigari, L. E., Beacom, J. F., Walker, T. P., & Zhang, P. 2005, *JCAP*, **2005**, 017
 Strotjohann, N. L., Kowalski, M., & Franckowiak, A. 2019, *A&A*, **622**, L9
 Tamborra, I., & Ando, S. 2016, *PhRvD*, **93**, 053010
 Thompson, T. A., Burrows, A., & Pinto, P. A. 2003, *ApJ*, **592**, 434
 Tipping, M. E., & Bishop, C. M. 1999, *J. Royal Stat. Soc. Ser. B*, **61**, 611
 Van Der Walt, S., Colbert, S. C., & Varoquaux, G. 2011, *CSE*, **13**, 22
 Woosley, S., & Janka, T. 2005, *NatPh*, **1**, 147